Time-Dependent Decrease in Fault Strength in the 2011–2016 Ibaraki-Fukushima Earthquake Sequence

Sam Wimpenny[1,2*], Natalie Forrest[1,2+] and Alex Copley[1]

[1]COMET, Bullard Laboratories, Department of Earth Sciences, University of Cambridge, UK

[2]COMET, Department of Earth and Environment, University of Leeds, UK

Emails: *earswi@leeds.ac.uk and +eenlef@leeds.ac.uk

Abstract

Two near-identical M_w 5.8 earthquakes in 2011 and 2016 ruptured the Mochiyama Fault in the Ibaraki-Fukushima region of Japan. The unusually short repeat time between the two earthquakes provides a rare opportunity to estimate the evolution of stress on a fault through an earthquake cycle, as the stress drop in the first earthquake provides a reference value from which we can infer variations through time in the stresses required to cause earthquake rupture. By combining observations of crustal deformation from GPS, InSAR and seismology with numerical models of stress transfer due to coseismic deformation and postseismic relaxation, we demonstrate that the rupture area on the Mochiyama Fault could only have been re-loaded by up to 50–80% of the 2011 earthquake stress drop (3–10 MPa) between that event and the subsequent 2016 earthquake. Most of this reloading was caused by afterslip around the rupture area driven by stress changes from the 2011 Mochiyama and Tohoku-oki earthquakes. We therefore infer that the Mochiyama Fault became weaker in the intervening 6 years, with at least a 1–5 MPa drop in the shear stresses needed to break the fault in earthquakes. The mechanism(s) that led to this weakening are unclear, but were associated with extensive aftershock seismicity that released a cumulative moment similar to the 2011 mainshock. Temporal changes in fault strength may therefore play a role in modulating the timing of moderate-magnitude earthquakes.

This paper is a pre-print, therefore has not finished peer review and is currently being considered for publication in Geophysical Journal International.

1 Introduction

Earthquakes are generated by the accumulation of elastic strain around a fault zone, and its eventual release when the shear stress resolved on the fault exceeds the frictional resistance to slip [Reid, 1910]. However, a deterministic application of this 'elastic rebound theory' to estimate the timing of large earthquakes has proven difficult [e.g. Roeloffs and Langbein, 1994], because the absolute state of stress on faults cannot be easily measured, the evolution of stress and strain between earthquakes is typically too long to be inferred from geodetic measurements of deformation, and the strength of active faults, and how fault strength varies in space, remain controversial topics. In addition, where the timing of multiple earthquakes on a particular fault patch are well documented, they sometimes show non-periodic repeat times [Murray and Segall, 2002; Sieh et al., 2008; Fukushima et al., 2018]. This observation suggests that the rate of fault loading, or alternatively the fault strength, may also vary with time to produce 'non-characteristic' earthquakes on some faults [Kagan et al., 2012].

Two near-identical M_w 5.8 normal-faulting earthquakes near Mochiyama in the Ibaraki-Fukushima region of Japan on the 19th March 2011 and 28th December 2016 provide a rare opportunity to determine the evolution of stress on a fault through a whole earthquake cycle (Figure 1). A previous study of the slip distributions in the Mochiyama earthquakes demonstrated that the two events ruptured the same area of the NNW-SSE striking Mochiyama Fault between the surface and 7 km depth (Figure 1b,c) [Fukushima et al., 2018; Komura et al., 2019]. Therefore the same patch of fault reached its failure stress twice in the space of ∼6 years. Between the two earthquakes, Japan's GEONET GPS network captured significant extensional strain localised across the Mochiyama Fault. Fukushima et al. [2018] argued that this deformation may reflect rapid reloading of the fault through extensive postseismic afterslip caused by the coseismic stress changes from the 2011 Mochiyama earthquake and the postseismic stress changes following the 2011 Tohoku-oki earthquake. However, they found that a model in which afterslip was driven by these stress changes could only account for a small fraction of the observed inter-event strain, and could only reload the Mochiyama Fault by less than 10–20% of the coseismic stress drop.

The Mochiyama earthquakes formed part of a sequence of seismicity in the Ibaraki-Fukushima region that began after the 11th March 2011 M_w 9.1 Tohoku-oki earthquake, and which included three other moderate-magnitude earthquakes within 20 km of Mochiyama in March and April 2011 [Imanishi et al., 2012; Fukushima et al., 2013] (Figure 1a). These earthquakes generated coseismic displacements that will have also changed the stress state on the Mochiyama Fault [King et al., 1994]. The stress changes will have been at least partially relaxed through afterslip and aftershocks within the seismogenic crust, and distributed viscous flow or localised viscous shear within the aseismic lower crust and upper mantle [Freed, 2005], causing time-dependent loading of the Mochiyama Fault between 2011 and 2016. As all of these stress changes were not included in the original calculations of Fukushima et al. [2018], and because their calculations could not account for the observed deformation, it remains unclear whether the Mochiyama Fault was fully reloaded back to its former failure stress, or whether the fault became weaker and ruptured at a lower failure stress in 2016. Addressing this question is clearly critical to developing our understanding of the controls on the strength of active faults and for building deterministic models of the earthquake cycle and seismic hazard.

In this study, we build upon the work of Fukushima et al. [2018] and determine the coseismic and time-dependent stress changes on the Mochiyama Fault through the Ibaraki-Fukushima earthquake sequence. We then use these stress change calculations to investigate potential temporal changes in the stresses required to break the fault in earthquakes. We begin by making new geodetic and seismological observations of the earthquake sequence in Section 2 to place constraints on the mechanisms that loaded the Mochiyama Fault. We then develop a series of forward models in Section 3 to determine by how much each different mechanism could have reloaded the Mochiyama Fault within the limits of the observed deformation. These models extend the previous work of Fukushima et al. [2018] by: (1) gaining more general insight into the ways postseismic relaxation reloads fault zones, and (2) by performing a wide range of models that allow us to assess how variations in the rheology of the Earth might translate into estimates of fault reloading and surface strain. From our modelling we find that the Mochiyama Fault could only have been reloaded by up to 50–80% of the coseismic stress drop of the 2011 earthquake by the time the 2016 earthquake re-ruptured the fault. In Section 4, we discuss the implications of this result for the time-dependent strength of active faults.

2 Observations of the Ibaraki-Fukushima Earthquake Sequence

2.1 Long-Period Body-Waveform Modelling

We first determined the focal mechanisms, centroid depths, source-time functions and moment releases of the 2011 and 2016 Mochiyama earthquakes by inverting their long-period teleseismic P and SH seismograms using synthetic waveforms of the P, S, pP, sP and sS phases, modelled assuming a finite-duration rupture at a point source [Nabalek, 1984; Zwick et al., 1994]. This method has been widely used and described, because of its sensitivity to the mechanisms and centroid depths of shallow moderate-magnitude earthquakes [e.g. McCaffrey and Abers, 1988; Taymaz et al., 1990]. Therefore further details of the modelling are provided in Supplementary Text S1.

The long-period waveforms of both earthquakes can be well matched at most stations using this method (Figure 2). The minimum-misfit solution for the 2011 earthquake has a seismic moment of 4.7×10^{17} Nm (M_w 5.7), a source-time function length of 3 seconds, a strike/dip/rake of the south-west dipping nodal plane of 295/51/-109 and a 5 km centroid depth (Figure 2a). The moment is similar to estimates from the USGS W-Phase (4.3×10^{17} Nm), USGS body-wave (4.5×10^{17} Nm) and Global Centroid Moment Tensor (6.9×10^{17} Nm) methods, but is only 40% of that derived from the InSAR-based coseismic slip inversion of Fukushima et al. [2018] (1.2×10^{18} Nm) when calculated using the same shear modulus. The 2016 earthquake has a near-identical minimum-misfit solution, with a moment release of 5.4×10^{17} Nm, a source-time function length of 4 seconds, a strike/dip/rake of 295/51/-100 and a centroid depth of 4 km (Figure 2b). The seismic moment estimate is identical to the geodetic moment derived by Fukushima et al. [2018] (5.4×10^{17} Nm) when using the same shear modulus. For both earthquakes, the centroid depth and moment release trade-off against one another, as at shallower depths the depth-phases destructively interfere with the direct phase meaning a larger moment is needed to account for waveforms of a given amplitude [Christensen and Ruff, 1985; Taymaz et al., 1990]. By varying the centroid depth during the inversions between 3 and 7 km, which is the InSAR-derived range of peak coseismic slip (Figure 1b,c), the minimum-misfit moment release in both earthquakes ranges from 3–6×10^{17} Nm.

Given that the amplitude of postseismic deformation scales with the coseismic moment [Churchill et al., 2022], our new estimate of the coseismic moment of the 2011 Mochiyama earthquake will have important implications for the predicted postseismic deformation. The likely explanation for the difference between the seismic and geodetic moment estimates is that the interferograms used by Fukushima et al. [2018] to invert for the pattern of slip in the 19th March 2011 Mochiyama earthquake (which span the dates 2011/02/02–2011/03/20 for the ascending track and 2010/11/20–2011/04/07 for the descending track) contain some surface deformation that was not caused by coseismic slip. One possible source of deformation was a series of shallow M_w 4–5 earthquakes within the fault's hangingwall that were triggered by the 11th March Tohoku-oki earthquake [Fukushima et al., 2018]. These small earthquakes align on a north-east dipping conjugate plane seen in the relocated aftershock seismicity (Supplementary Figure 1). By mapping the surface deformation from these small, shallow earthquakes into deep coseismic slip on the Mochiyama Fault, Fukushima et al. [2018] could have overestimated the coseismic moment release in the 19th March Mochiyama earthquake. The interferograms used to invert for the pattern of coseismic slip may also contain some surface deformation caused by early postseismic slip, which would also lead to an overestimate of the coseismic moment release [e.g. Twardzik et al., 2019]. In the following sections, we show that the GPS and microseismicity measurements support the conclusion that the moment release in 19th March 2011 earthquake derived from the slip inversion of Fukushima et al. [2018] is an overestimate.

2.2 GPS

We collected the F3 solutions of daily position time-series for each GPS station in Japan's GEONET network and used a trajectory-modelling approach [e.g. Bedford et al., 2020] to fit the observed displacements with an arbitrary combination of steps, linear ramps, logarithmic terms and sinusoids using a non-linear least-squares routine implemented in SciPy [Virtanen et al., 2020]. After the first attempt to fit the time-series, we stacked the residuals between the trajectory models and the observed time-series at every station to determine the common-mode error and removed it from the observed time-series [Wdowinski et al., 1997]. We then fit these corrected time-series with an updated trajectory model, yielding a smooth approximation of the displacement through time at each GPS station. Final residuals between the trajectory models and the corrected displacement time-series, which we interpret to represent random noise that is not caused by tectonic deformation, were consistently Gaussian with a standard deviation of 2–3 mm and a mean of 0 mm.

The vertical and horizontal displacements are dominated by an eastward translation and uplift caused by postseismic relaxation after the Tohoku-oki earthquake. Therefore, to determine the evolution of deformation in the study region, we calculated the 2-D incremental strain tensor over different epochs using the triangular interpolation method of Bourne et al. [1998] and the trajectory models of the displacements. This method does not enforce any spatial smoothing on the strain field, therefore can identify strain signals on the length scale of the station spacing. The noise levels in the displacement measurements translate into an uncertainty of ∼0.2–0.3 microstrain in the strain measurements, given the typical station spacing in the network of 15–20 km. The vertical displacements do not contain any clear signals related to the Ibaraki-Fukushima earthquake sequence beyond those associated with the coseismic displacements in the Tohoku-oki and Iwaki earthquakes, and therefore we do not consider them further here.

On the 19th March 2011 the first earthquake to rupture the Mochiyama Fault generated predominantly

1.6 microstrain of NE-SW to ENE-WSW extension in the triangles spanning the fault zone, and predominantly 1 microstrain contraction in triangles to the south-west of the fault (Figure 3a). A forward calculation of the coseismic strain predicted by the slip model of Fukushima et al. [2018] can match the pattern of the observed strain, but significantly over-predicts the strain amplitude (Supplementary Figure 2a). Therefore we performed a grid search of coseismic slip models in which we applied a scaling factor to the slip distribution, and searched for the models that best fit the coseismic strain field. We found that models with a moment release of 5–6$\times10^{17}$ Nm best fit the strain observations (Supplementary Figure 2b), which is consistent with the moment release determined by the long-period body-waveform modelling presented in Section 2.1 (3–6$\times10^{17}$ Nm).

In the month that followed the 2011 Mochiyama earthquake, the GPS network recorded a further 1.2 microstrain of NE-SW postseismic extension across the Mochiyama Fault (Figure 3b), and 4–5 microstrain of NW-SE extension generated by a M_w 5.9 normal-faulting earthquake on the 23rd March 2011 [Fukushima et al., 2013] (Figure 3b). Outside of the epicentral region of these earthquakes, the Ibaraki-Fukushima area was being stretched ~E–W by 0.2–0.4 microstrain as a result of ongoing postseismic relaxation following the Tohoku-oki earthquake [Hu et al., 2016].

The largest earthquake within the sequence occurred on the 11th April 2011: a M_w 6.6 earthquake that simultaneously ruptured two NW-SE trending normal faults 20 km north of Mochiyama near the city of Iwaki (known herein as the 'Iwaki Faults'). The Iwaki earthquake was followed a day later by a M_w 5.9 strike-slip aftershock. These two earthquakes generated 20–25 microstrain of extension across the Iwaki Faults and 0.7 microstrain of extension across the Mochiyama Fault (Figure 3c).

Between May 2011 and December 2016 there were no more $M_w > 5$ earthquakes in the study area. GPS stations that span the Mochiyama Fault measured 2–3 microstrain of ENE-WSW extension (Figure 3d) that followed a logarithmic decay in time. Elsewhere, almost all of the study region experienced ~2 microstrain of shear with the maximum principal strain axis being oriented ~E-W to NW-SE, and the minimum principal strain axis oriented ~N-S to NE-SW. This regional pattern of shear strain represents the deformation of the Japanese mainland caused by postseismic relaxation following the Tohoku-oki earthquake [e.g. Hu et al., 2016; Becker et al., 2018].

The cumulative strain between the 2011 and 2016 Mochiyama earthquakes (the 'inter-event period') represents the horizontal surface strain associated with reloading of the Mochiyama Fault (Figure 3e). The strain across the fault consisted of 3.8–4.3 microstrain of extension — 0.7 microstrain of which can be attributed to the static deformation caused by the Iwaki earthquakes. Any model of the reloading of the Mochiyama Fault must account for the remaining 3.1–3.6 microstrain of observed across-fault stretching through aseismic deformation mechanisms. Within the triangles to the south-west of the fault that span the fault's hangingwall, the strain field records incremental contraction. Notably, the orientation of the principal strain axes in triangles that span the Mochiyama Fault, and triangles in the immediate fault hangingwall, are sub-parallel to the principle axes of the coseismic strain field in the 2011 Mochiyama earthquake (compare Figure 3a with 3e). Therefore, the sense of aseismic strain around the Mochiyama Fault over the inter-event period can be accounted for by postseismic aseismic slip ('afterslip') on the mainshock fault plane within a similar depth-range to coseismic slip.

On the 28th December 2016 the second earthquake re-ruptured the Mochiyama Fault and generated 2 microstrain of ENE-WSW to NE-SW extension across the fault zone with a similar pattern to the 2011 earthquake (Figure 3f). The across-fault extension in 2016 was slightly larger than in 2011, which supports the conclusion from the long-period body-waveform modelling that the 2016 earthquake had a slightly larger moment release than in 2011. Over the postseismic period between December 2016 and December 2017, the GPS network captured ∼0.3 microstrain of logarithmically-decaying postseismic extension across the Mochiyama Fault (Supplementary Figure 3), which was 10-times smaller than the strain recorded in the year after the 2011 earthquake. Despite the stark difference in the amplitude of the postseismic strain measured after the 2011 and 2016 Mochiyama earthquakes, the relaxation time of the strain transients were near-identical (Supplementary Figure 4).

In the 6 years prior to the Mochiyama and Tohoku-oki earthquakes (2005–2011), the strain field across the Mochiyama Fault consisted of 1–2 microstrain of simple shear with the minimum principle axis of strain oriented ∼N-S to NW-SE (Supplementary Figure 3a). This interseismic strain is not consistent with signals produced by localised shear down-dip of the rupture area, which could load the Mochiyama Fault towards failure (see further discussion in Section 3.2). On the 11th March 2011, coseismic slip in the Tohoku-oki earthquake led to E-W stretching of the region around the Mochiyama Fault by 10 microstrain (Supplementary Figure 3b), and was followed by a further 0.4 microstrain of ∼E-W stretching between the 11th and 18th March (Supplementary Figure 3c), which will have loaded the Mochiyama Fault towards failure [Ozawa et al., 2011].

2.3 Radar Geodesy

Fukushima et al. [2018] and Komura et al. [2019] previously formed ALOS interferograms of the co-seismic deformation in the 2011 and 2016 Mochiyama earthquakes (Figure 4a,c). The two earthquakes generated near-identical patterns of coseismic surface deformation, suggesting the slip distributions overlapped significantly at depth. The interferograms record peak line-of-sight (LOS) displacements of 40–60 cm and a sharp offset in LOS across the north-western fault tip. The LOS displacements decrease in amplitude, and become smoother, towards the south-eastern fault tip. These features of the data suggest that peak slip in both earthquakes overlapped on the north-western portion of the fault, and that slip became buried and decreased towards the south-east [Fukushima et al., 2018] (see Figure 1b,c). Given that both earthquakes had similar seismic moment release, and similar rupture areas, then it is likely that they had similar stress drops.

For the 2011 Mochiyama earthquake, the coseismic interferogram in Figure 4a shows an increase in the wavelength of the hangingwall subsidence towards the southern edge of the fault. This is the same area that experienced shallow M_w 4 and 5 normal-faulting foreshocks between the 11th March and 19th March 2011, which may have contributed to the surface deformation measured by InSAR [Fukushima et al., 2018].

To measure the postseismic deformation around the Mochiyama Fault we formed Envisat ASAR interferograms from the descending track 347, which start from the 21st March 2011 (2 days after the mainshock) and cover the first 7 months after the 2011 Mochiyama earthquake. Envisat stopped transmitting data at the end of 2011, therefore we could only measure the early postseismic deformation. The SAR data was processed using ISCE and a 30 m SRTM Digital Elevation Model [Farr et al., 2007] to remove the topographic contribution to phase. The interferograms were unwrapped using the statistical-cost network flow algorithm SNAPHU [Zebker and Lu, 1998]. We also applied a Gaussian filter to the interferograms with a half-width of 0.5 km and removed a planar ramp.

Much of the region around the Mochiyama Fault is covered in thick vegetation, and therefore the C-band data suffered from decorrelation. Nevertheless, in the first 2–32 days following the 2011 Mochiyama earthquake one postseismic interferogram with good coherence could be formed (Figure 4b). A step of 4–5 cm in LOS displacement can be seen across the surface trace of the Mochiyama Fault. The sharp offset in LOS displacement is mainly concentrated to the south-east of the area of peak coseismic LOS displacement, which is a common observation following normal-faulting earthquakes and reflects afterslip on the shallow portion of the mainshock rupture plane [e.g. Cheloni et al., 2010]. At distances of ∼5–10 km from the fault, the relative LOS displacements across the fault are <1–2 cm, which limits the amount of deep afterslip or ductile flow that occurred in the first month after the 2011 earthquake.

We also formed interferograms using Sentinel-1 SAR data covering the first 4–28 days of postseismic deformation following the 2016 Mochiyama earthquake, using the same processing work flow. The Sentinel-1 measurements reveal a sharp $\sim$2 cm step in LOS displacement across the fault, and $<$1 cm of relative LOS displacement at distances $>$5 km from the surface trace of the fault (Figure 4d). The patterns of near-field postseismic deformation are similar in the first month following the two earthquakes. However, the 2016 earthquake was followed by less shallow afterslip.

2.4 Aftershock Seismicity

The locations, magnitudes and focal mechanisms of small earthquakes provide additional constraints on the deformation in the region of the Mochiyama Fault. We use the hypocentral locations determined by Uchide and Imanishi [2018], which are based on the Japan Meteorological Agency (JMA) unified catalogue that have been relatively re-located using the double-difference method [Waldhauser and Ellsworth, 2000]. Focal mechanisms derived by the National Research Institute for Earth Science and Disaster Resilience (NIED) provide additional constraints on the sources of microseismicity.

The 2011 Mochiyama earthquake was followed by a large number of normal-faulting aftershocks (Figure 5a) concentrated almost entirely between 5 km and 10 km depth (Supplementary Figure 5). The aftershocks were clustered around the margins and base of the rupture area, and delineate a planar structure dipping 40–60° towards the south-west [Kato et al., 2011]. Aftershocks recorded in the 2 years following the 2016 Mochiyama earthquake also had mostly normal-faulting mechanisms (Figure 5b), and were concentrated beneath the down-dip edge of the rupture area (Supplementary Figure 5). The similarity between the aftershock and the mainshock mechanisms, and the alignment of the microseismicity with the along-strike and down-dip projection of the mainshocks, imply that the aftershocks reflect slip on the Mochiyama Fault around the margins of the coseismic rupture.

Although the mechanisms and magnitudes of the 2011 and 2016 Mochiyama earthquakes were similar, the moment release in their aftershock sequences was significantly different (Figure 5c-f). The first six months after the 2011 earthquake was characterised by aftershock moment release that followed a logarithmic decay, mirroring the across-fault strain measured by the GPS network (Figure 5c,e). Most unusually, though, was that the cumulative moment release from aftershocks in the region directly around the Mochiyama Fault in the period May 2011 to December 2016 was $6 \pm 2 \times 10^{17}$ Nm, which is similar in magnitude to the 2011 mainshock moment release (3–$6{\times}10^{17}$ Nm). Aftershock sequences typically only account for between 1% and 20% of the mainshock moment [Zakharova et al., 2013], suggesting the seismicity that followed the 2011 Mochiyama earthquake was unusually energetic. The 2016 earthquake was followed by little across-fault extensional strain (Figure 5d) and a less energetic aftershock sequence that released only $1.8 \pm 0.8 \times 10^{17}$ Nm within 2 years of the mainshock (Figure 5f), which equates to a third of the mainshock moment release.

2.5 Summary of the Key Observations

The InSAR and body-waveform modelling show that the 2011 and 2016 earthquakes ruptured the same area of the Mochiyama Fault in two earthquakes with near-identical magnitudes. Over the inter-event period between these two earthquakes, the GPS network captured 3.1–3.6 microstrain of across-fault extension that could not be attributed to any moderate-magnitude seismicity. In GPS triangles that span the fault hangingwall, the sense of strain over the inter-event period was contractional. Postseismic InSAR observations demonstrated that some of this strain derived from at least ~4–5 cm of shallow afterslip above the coseismic rupture on the Mochiyama Fault. Extensive aftershocks around the margins of the coseismic rupture suggest that fault slip was also prevalent at depth, extending down to at least 10 km. Summing the aftershock moment release over the aftershock cloud implies there was at least 20 cm of slip beneath the coseismic rupture over the inter-event period. Beneath 10 km there were few aftershocks, indicating that any deformation was accommodated predominantly by aseismic deformation mechanisms. Notably, the amplitude of the postseismic across-fault extension following the 2016 earthquake was 10-times smaller than following the 2011 earthquake. In the next section, we develop models of slip and stress on the Mochiyama Fault between the 2011 and 2016 earthquakes that attempt to explain these observations.

3 Modelling Stress Changes on the Mochiyama Fault

The observations point to three major sources of deformation in the Ibaraki-Fukushima region between the Mochiyama earthquakes: (1) postseismic relaxation on and around the Mochiyama Fault, (2) coseismic deformation and postseismic relaxation from the nearby Iwaki earthquakes, and (3) regional postseismic relaxation following the Tohoku-oki earthquake. Most of the GPS measurements are too far from the fault, and there are too few coherent interferograms, to constrain kinematic inversions for the distribution of aseismic slip and viscous flow around the Mochiyama Fault [e.g. Murray and Segall, 2002; Muto et al., 2019]. We therefore take a forward-modelling approach to calculate how each source of deformation could have contributed to the pattern of surface strain, and the stress changes on the Mochiyama Fault, following the 2011 Mochiyama earthquake.

The time-series of deformation from the GPS and aftershock moment release indicate that the majority of the postseismic transient visible at the surface had finished by the time of the 2016 Mochiyama earthquake, suggesting that most of the coseismic stress changes imposed on the crust surrounding the fault had been relaxed, or balanced by elastic resistance to deformation in the seismogenic layer. We therefore keep the models as general as possible by calculating this 'fully-relaxed' state, and by fitting the pattern and amplitude of strain across the Mochiyama Fault, but not the temporal evolution of the strain. Considering only the fully-relaxed model has the benefit of making the estimates of reloading insensitive to the form of the constitutive laws that govern postseismic relaxation. The calculations will, however, yield upper bounds on the amount of fault zone reloading. It is possible that some fraction of the stress changes are relaxed by deformation mechanisms with a relaxation time that is longer than the inter-event period of $\sim$6 years, in which case the reloading will be smaller than our estimates below.

We also make the simplification that the background loading rate of the fault (the 'interseismic deformation') is small over the short time-frame between the two earthquakes, which is consistent with: (1) the lack of observed interseismic strain build around on the Mochiyama Fault during 2005–2011 (Supplementary Figure 3a), (2) the lack of moderate-magnitude seismicity in the 50 years prior to the Mochiyama earthquakes in the gCMT catalogue [Dziewonski et al., 1981; Ekström et al., 2012], and (3) the paleoseismic record [Komura et al., 2019]. With these simplifications, it is the geometries of the imposed stresses and rheological components of the model domain, and the styles of postseismic relaxation, that control the magnitude of the fault reloading.

3.1 Generalised Models of Postseismic Reloading

To first gain an understanding of how local postseismic relaxation may have reloaded the Mochiyama Fault, we built a set of generalised stress-driven models that link coseismic slip to the postseismic reloading of the rupture area [e.g. Ellis and Stöckhert, 2004; Bagge and Hampel, 2017]. The models were designed to capture the maximum contribution of the three main postseismic deformation mechanisms — afterslip, localised viscous shear and distributed visco-elastic relaxation — to reloading a normal fault after an earthquake [e.g. Freed and Lin, 1998]. The models also allow us to explore how uncertainties in our knowledge of the rheology of the crust and upper mantle in the study region will translate into uncertainties in the estimate of reloading of the Mochiyama Fault.

The model setup consists of a planar dip-slip fault of along-strike length L in a linear elastic layer of thickness z_e, which overlies a visco-elastic half-space (Figure 6). The elastic layer represents the seismogenic layer in the Earth in which elastic strain can accumulate and remain stored for the duration of an earthquake cycle. The visco-elastic half-space represents the depth below which the crust and mantle is hot enough that viscous creep can relax elastic stresses over an earthquake cycle. Spatially-uniform coseismic slip on the fault extends from the surface down to a depth z_r, and generates static stress changes in the surrounding medium. These static stress changes are then relaxed by viscous flow at depths $z > z_e$ and by afterslip at depths $0 \leq z \leq z_e$. In the fully-relaxed state, the afterslip zone down-dip of the coseismic rupture also approximates the behaviour of a thin (<200 m-wide given the model discretisation) viscous shear zone surrounded by elastic wall rocks, therefore also represents the case where deformation in the lower crust is accommodated in shear zones and not by distributed flow. The coseismic rupture remains locked and cannot slip post-seismically, therefore accumulates elastic strain and is reloaded as the surrounding regions deform.

The condition for frictional failure on a fault is described by the Coulomb criterion: $\tau - \mu'\sigma = 0$, where μ' is the effective coefficient of friction, τ is the shear stress and σ is the fault-normal stress (+ve for fault clamping) [Byerlee, 1978]. During coseismic slip the shear stress drops by $\Delta\tau_c$, whilst the normal stress change $\Delta\sigma_c$ is negligible. In order for the fault to reach its failure condition again following postseismic stress changes $\Delta\tau_p$ and $\Delta\sigma_p$ requires the following condition to be satisfied:

$$\underbrace{\frac{\Delta\tau_p}{\Delta\tau_c} - \mu'\left(\frac{\Delta\sigma_p}{\Delta\tau_c}\right)}_{\text{Stress Changes}} + \underbrace{\Delta\mu'\left(\frac{\sigma}{\Delta\tau_c}\right)}_{\text{Strength Changes}} \simeq 1, \tag{1}$$

assuming that $\Delta\sigma_p \ll \sigma$ (see Supplementary Text S2 for derivation). Equation 1 shows that the stress changes on the fault are primarily a product of two effects: the postseismic shear stress change relative to the coseismic shear stress drop $\Delta\tau_p/\Delta\tau_c$ (the 'shear stress recovery') and the postseismic change in fault-normal stress relative to the coseismic shear stress drop $\Delta\sigma_p/\Delta\tau_c$ (the 'fault clamping'). Changes in the frictional strength of the fault surface $\Delta\mu'$ may also contribute by reducing the fault stress needed for failure (the 'strength change' term in Equation 1). We evaluate the terms $\Delta\tau_p/\Delta\tau_c$ and $\Delta\sigma_p/\Delta\tau_c$ from our numerical models, and not the more common metric of Coulomb stress ($\Delta\tau_p - \mu'\Delta\sigma_p$), to explicitly separate reloading due to changes in fault stress from the effects of fault strength. From this analysis, we can isolate the size of the strength change term, which we discuss in detail in Section 4.

We calculated $\Delta\tau_c$, $\Delta\tau_p$ and $\Delta\sigma_p$ using the Computational Infrastructure for Geodynamics code RELAX, which solves for the quasi-static deformation in elastic and visco-elastic media in response to fault slip using an equivalent body-force approach [see Barbot et al., 2009; Barbot and Fialko, 2010b,a]. We used a 102 km-wide domain with a discretisation of 0.2 km to ensure that models accurately resolved the gradients in strain and stress near the edges of the coseismic rupture. Fault slip was also tapered at the margins of each fault patch to dampen stress singularities. The boundaries of the model domain were set to be at least $5L$ (∼50 km) away, so that the periodicity in the solutions for displacement and stress introduced by the discrete Fourier transform that RELAX uses had little effect on the model results. After calculating the coseismic stress changes for the given coseismic slip distribution, the models were run for 5 relaxation times to approximate the fully-relaxed state.

3.1.1 Results of the Generalised Modelling

We ran nine sets of forward calculations, varying the deformation mechanism (visco-elastic only, afterslip only and coupled afterslip + visco-elastic), the coseismic fault slip u, the depth of the coseismic rupture relative to the elastic layer thickness z_r/z_e and the along-strike length of the coseismic rupture L. We found that varying the along-strike length of fault that is able to slide through afterslip L_f had little effect on the estimates of fault reloading when $L_f > 5$ km (Supplementary Figure 6), therefore we fixed L_f to 5 km in all models. All other parameters, such as the elastic properties of the seismogenic layer, were held constant. The results of the modelling, expressed in terms of shear stress recovery $\Delta\tau_p/\Delta\tau_c$, are shown in Figure 7. The equivalent results for the fault clamping $\Delta\sigma_p/\Delta\tau_c$ are shown in Supplementary Figure 7, but are not discussed further in the main text as they make a relatively minor ($\ll$5%) contribution to the reloading when scaled by the effective friction μ' on earthquake-generating faults (0.01–0.4; see Toda et al. [2011]; Copley [2018]; Collettini et al. [2019]).

Models that only allow stress changes to be relaxed through viscous flow beneath the elastic layer consistently show that the shear stress recovery is largest at the base of the elastic layer and decreases non-linearly towards the surface (Figure 7a-c). Shear stress recovery is also largest within the centre of the rupture, and smallest along its edges. These first-order patterns are a result of the postseismic strain within the elastic layer being largest at its base, where the coseismic stress changes are largest and will have driven the most viscous flow. The postseismic strains and stress changes decay into the elastic layer, as the layer resists deformation from viscous flow below. Varying the amount of fault slip has no effect on the shear stress recovery, and varying the rupture length has only a small effect on shear stress recovery. Changing the fault slip does not alter the shear stress recovery because increasing fault slip causes a proportional increase in the amount of viscous flow needed to relax the coseismic stress change, and therefore a proportional amount of fault reloading. The depth of the rupture relative to the elastic layer thickness is the dominant control on the fault reloading, with shear stress recovery increasing significantly as the rupture depth approaches the elastic layer thickness. Nevertheless, even when the fault ruptures to the base of the elastic layer, the shear stress recovery remains less than 40% of the coseismic stress drop at the base of the rupture, and less than 10% at the surface.

Models that only allow stress changes to be relaxed through afterslip show a different pattern of reloading (Figure 7d-f). Shear stress recovery is largest along the edges of the coseismic rupture and within the shallowest part of the elastic layer. Again, the shear stress recovery is independent of the amount of coseismic slip, but does depend on the down-dip extent of the coseismic rupture relative to the elastic layer thickness and the along-strike length of the rupture area. These patterns indicate that the larger the area that surrounds the rupture that is able to slip in response to coseismic stress changes, the more this area is able to slide postseismically before elastic resistance from the surrounding rocks balances the stresses driving slip. Afterslip only leads to a shear stress recovery of <30% of the coseismic stress drop on any particular part of the rupture.

Models that include mechanically-coupled afterslip and visco-elastic relaxation generate the largest shear stress recovery on the rupture area (Figure 7g-i). Viscous flow can load the base of the coseismic rupture whilst afterslip can load the edges and top of the rupture. Shear stress recovery of 45% the coseismic stress drop occurs along the edges of the rupture, whilst in the shallow part of the elastic layer the maximum shear stress recovery is 20%.

These calculations demonstrate that postseismic relaxation around the margins of a $\sim M_w$ 6 rupture can only partly reload the rupture area. Variations in the depth of the coseismic rupture relative to the thickness of the seismogenic layer, the area of the rupture and afterslip region, and the deformation mechanisms that contribute to postseismic relaxation, will all influence the shear stress recovery, but these cannot increase the shear stress recovery beyond 45%. This result is perhaps unsurprising, given that most faults rupture after hundreds to thousands of years without an earthquake, which indicates that slow interseismic strain accumulation makes up the remainder of the stress deficit on most active faults. In the next section, we apply these models to the Mochiyama earthquakes and compare them with the observed surface deformation.

3.2 Specific Models of Stress Changes on the Mochiyama Fault

To model the stress changes specific to the Mochiyama Fault, we used the slip distribution of Fukushima et al. [2018] projected onto a planar approximation of the Mochiyama Fault with the geometry defined by the relocated seismicity and surface ruptures. In Section 2, we showed that the slip model of Fukushima et al. [2018] overestimates the amount of coseismic moment release, but the general distribution of slip is likely to be accurate given that it matches the along-strike length and across-strike width of the LOS displacement pattern measured by InSAR. We therefore scaled the amount of slip such that it matches the moment release calculated from body-waveform modelling and the coseismic strain from GPS measurements (Supplementary Figure 2). With this modification, the slip distribution has a peak slip of 0.6 m, an average shear stress drop $\Delta\tau_c$ of 3 MPa and a peak shear stress drop of 8 MPa in the centre of the rupture. The spatial variability in the stress drop is a result of high slip gradients within the core of the rupture area, and constant slip gradients along the margins of the rupture [Fukushima et al., 2018]. We explore how uncertainties in the slip distribution could effect the estimates of fault reloading later in this section.

We calculated the postseismic reloading of the rupture area by allowing the coseismic stress changes to be relaxed by afterslip on the mainshock fault plane around the margins of the rupture, which spans the area that experienced normal-faulting aftershocks with nodal planes parallel to the mainshock (Figure 5a,b). Coseismic stress changes below 10 km are either relaxed by distributed viscous flow, or by localised shear in a shear zone that follows the down-dip projection of the mainshock fault plane. The depth of the transition in deformation mechanism was chosen on the basis of the sharp cut-off in microseismicity at 10 km depth (Supplementary Figure 1). We consider this elastic layer thickness to be a lower bound, and will therefore provide an upper bound on the estimate of the reloading caused by distributed viscous flow. If the elastic layer were thicker, then the estimated reloading in models that include viscous flow would be lower.

The predicted deformation is highly localised around the fault (Figure 8a,b), and only the strain measured by GPS triangles that span the fault, or are just to the south-west of the fault trace in the immediate fault hangingwall, show strain amplitudes larger than the measurement uncertainty (0.2–0.3 microstrain). We therefore focus on comparing the modelled and observed deformation in these triangles.

Models that both include, and exclude, distributed viscous flow at depths >10 km can match the observed pattern of postseismic strain during the inter-event period, with ENE-WSW to NE-SW extension in triangles that span the Mochiyama Fault. One of the key differences between the models is that deep viscous flow generates more across-fault extension (2.6 microstrain) than if only afterslip and localised viscous shear are allowed to relax the coseismic stress changes (0.7 microstrain). This difference reflects the fact that distributed flow at depth produces long-wavelength surface deformation that strongly affects the GPS sites that are 10–20 km from the fault. Nevertheless, both models still under-estimate the total amount of inter-event extension observed across the Mochiyama Fault (3.1–3.6 microstrain). GPS triangles to the south-west of the fault trace within the fault hangingwall show different patterns of strain for the different mechanisms of postseismic relaxation at depth. Afterslip beneath the rupture produces a small amount of incremental NE-SW extension, whilst distributed viscous flow produces incremental contraction that rotates in orientation from north to south that is more consistent with the observed pattern of inter-event strain (Figure 8a,b).

Despite the differences in the predicted surface strain, the models yield similar patterns of afterslip and fault reloading, with up to 80% shear stress recovery along the margins of the rupture and less than 10% within its interior (Figure 8c,d). The shear stress recovery along the margins of the rupture area is larger than in the spatially-uniform slip models shown in Section 3.1, because the margins of the rupture have a low coseismic stress drop when calculated using the distributed slip model, yet experience the largest postseismic stress changes. The shear stress recovery averaged over the rupture for models with and without visco-elastic relaxation are 33% and 28%, respectively, which is consistent with the average shear stress recovery in the generalised models that use a similar rheological structure (Figure 7e,h). As seen in the Section 3.1, viscous flow at depth has little effect on the shear stress recovery, because the fault did not rupture all the way to the base of the elastic layer. The modelled fault clamping $\Delta\sigma_p/\Delta\tau_c$ is everywhere <10% (Supplementary Figure 8), and therefore makes a negligible contribution to the reloading when scaled by the effective friction.

3.2.1 Effects of the Coseismic Slip Distribution on Reloading

The stress changes that drive postseismic relaxation are a function of gradients in the input slip model. Therefore, the smoothing used to regularise the inversions for coseismic slip, or the inclusion of some postseismic slip in the coseismic slip distribution, may have an effect on the predicted amplitude of postseismic deformation. To explore whether this effect can account for the difference between the modelled and observed inter-event strain across the Mochiyama Fault, we ran a series of calculations in which we artificially vary the smoothing of the input slip distribution in the 2011 earthquake by removing areas with slip less than some minimum value u_{min}, and then redistribute the remaining moment release evenly across the rupture area [e.g. Barbot et al., 2009]. This process leads to a compaction of the slip distribution, and an increase in the coseismic stress drop (Supplementary Figure 9), with a slight decrease in the fit between the observed and modelled coseismic surface deformation.

Models with more compact slip distributions and higher stress drops cause more postseismic relaxation and larger surface strains (Figure 9a). If all areas with slip <0.4 m are removed, which adjusts the average stress drop to be 10 MPa, then the models can account for the observed 3.1–3.6 microstrain of across-fault extension over the inter-event period. Nevertheless, compacting the slip distribution has little effect on the average shear stress recovery on the rupture (Figure 9b), because the coseismic stress drop also increases. The generalised calculations in Section 3.1.1 provide the physical explanation for this feature of the models: increased stress drop causes increased elastic strain within the surrounding crust, which itself leads to a proportional amount of fault zone reloading through postseismic relaxation. Therefore, although uncertainties in the roughness of the slip distribution of the 2011 earthquake can account for the discrepancy between the modelled and observed across-fault strain between the 2011 and 2016 Mochiyama earthquakes, the rupture area can still only be reloaded by on average $\lesssim$35% of the coseismic stress drop through postseismic relaxation (Figure 9b). A high coseismic stress drop also does not account for the significant difference in the amplitude of the postseismic strain observed following the 2011 and 2016 Mochiyama earthquakes. In the next section, we explore what contributions the static and time-dependent stress changes from the Iwaki earthquake sequence could have made to the reloading of the Mochiyama Fault.

3.2.2 Stress Changes from the Iwaki Earthquakes

We used the fault geometry and slip estimates from Fukushima et al. [2013] to calculate the co- and post-seismic displacements due to slip in the Iwaki earthquake sequence, and the resulting stress changes on the Mochiyama Fault. The modelled coseismic strain matches the strain observed by the GPS network, and can account for the 0.7 microstrain of extension across the Mochiyama Fault in April 2011 (Supplementary Figure 10). We find that the Iwaki earthquakes caused a <0.3–0.4 MPa increase in shear stress (Figure 10b) and a <0.2–0.3 MPa decrease in normal stress (Figure 10c) along the northern-most portion of the Mochiyama Fault. The amplitude of these static stress changes decrease significantly towards the southern edge of the Mochiyama Fault, as stress decays as the inverse cube of distance from the strain source in the elastic crust [Okada, 1992]. Therefore, although the Iwaki earthquakes did move the Mochiyama Fault closer to failure, they contributed a shear stress recovery of <5–10% of the coseismic stress drop (3–10 MPa; Figure 10a).

Postseismic relaxation on the Iwaki Faults could have produced up to 0.3–0.5 microstrain of extension across the Mochiyama Fault, which is ~10–15% of the observed inter-event extension. The stress changes oppose the initial static loading with a shear stress decrease of <0.2–0.3 MPa (Figure 10d) and a normal stress increase of <0.3–0.4 MPa (Figure 10e) along the base of the Mochiyama Fault. Models that do not include distributed viscous flow below 10 km depth predict negligible strain and stress changes on the Mochiyama Fault that are $\ll$0.1 MPa (Supplementary Figure 11). Mechanically-coupled models that include the co- and post-seismic stress changes in both events show that the Iwaki earthquakes will have only slightly inhibited afterslip on the northern half of the Mochiyama Fault, and could have reduced the average shear stress recovery by <2% (Figure 10f). Therefore, despite the proximity of the Iwaki earthquakes to Mochiyama, the static and time-dependent stress changes caused by the Iwaki earthquake sequence played a minor role in the reloading the Mochiyama Fault.

3.2.3 Stress Changes from the Tohoku-oki Earthquake

Coseismic slip in the 11th March 2011 Tohoku-oki earthquake horizontally stretched the overriding plate and caused widespread changes in the style and frequency of seismicity in the shallow crust of mainland Japan [Okada et al., 2011]. Seismicity in the study region prior to the Tohoku-oki earthquake consisted mostly of normal faulting [Imanishi et al., 2012], and the static stress changes from the Tohoku-oki earthquake were equivalent to a shear stress increase of 0.8 MPa and a normal stress drop of −1.2 MPa on the Mochiyama Fault (calculated from the model of Hu et al. [2016]). These stress changes did not immediately trigger rupture, but likely brought the Mochiyama Fault close to failure. Postseismic relaxation following the Tohoku-oki earthquake contributed additional loading of faults in mainland Japan [Becker et al., 2018]. Fukushima et al. [2018] calculated that afterslip on the megathrust around the Tohoku-oki rupture area would have subject the Mochiyama Fault to an increase in shear stress of 0.1 MPa and a decrease in fault normal stress of −0.2 MPa over the period March 2011 to December 2016. A more complex calculation by Hu et al. [2016], which includes the effects of visco-elastic relaxation beneath the crust, afterslip on the megathrust, and interseismic relocking of the subduction interface, suggests there may have been a shear stress increase of 0.07 MPa and a normal stress drop of −0.2 MPa on the Mochiyama Fault over the same period (Supplementary Figure 12). Both models predict stress changes that are small compared to the coseismic stress drop in the Mochiyama earthquake, and would directly contribute to $\ll$5% of the shear stress recovery on the rupture area.

The stress changes from the Tohoku-oki earthquake will have also influenced the pattern and amplitude of afterslip around the rupture area on the Mochiyama Fault [Fukushima et al., 2018]. We ran calculations that include the relaxation of both the coseismic stress changes due to the Mochiyama earthquake through localised afterslip, and the co- and post-seismic stress changes from the Tohoku-oki earthquake in the model of Hu et al. [2016] resolved on the Mochiyama Fault. We include the coseismic stress changes from the Tohoku-oki earthquake, as it is unlikely that a significant fraction of this stress imposed on the Mochiyama Fault was relaxed by the timing of the 2011 Mochiyama earthquake given that they were only 7 days apart. These calculations produce up to 2.0 microstrain of extension across the Mochiyama Fault by boosting the average amount of afterslip around the rupture area from ~20 cm to ~60 cm (Figure 11a). However, the orientations of the minimum principal strain axes in triangles that span the Mochiyama Fault are rotated anti-clockwise relative to strain axes measured by the GPS network, and the maximum principal strain axes in triangles in the fault hangingwall do not match the observed ~ENE-WSW contraction in these areas. These differences between the stress-driven models and observations can be accounted for if afterslip were constrained to have a similar rake to coseismic slip and occurred mostly on the top ~5 km of the Mochiyama Fault (Figure 11c,d).

The relaxation of stress changes caused by the Tohoku-oki earthquake by slip on the Mochiyama Fault (Figure 11a), along with the co- and post-seismic deformation in the nearby Iwaki earthquakes (Supplementary Figure 10), can therefore account for the majority of the extension measured by the GPS network over the inter-event period, and the order-of-magnitude difference in the amplitude of postseismic strain observed following the 2011 and 2016 Mochiyama earthquakes. When including the additional deformation caused by the stress changes in the Tohoku-oki earthquake, the average shear stress recovery on the mainshock rupture area increases to 40%, which is still only a fraction of that needed to entirely reload the rupture to its former failure stress.

3.2.4 Effects of a Prestress or Triggered Slip on Reloading

Pre-existing stresses around the rupture area on the Mochiyama Fault may have also been relaxed by aseismic slip or localised aseismic shearing within the down-dip shear zone during the inter-event period. For these pre-existing stresses to exist would require some mechanism that allows elastic strain to be stored in the rocks around the edge of the rupture area without being relaxed by aseismic slip, or during slip in the Mochiyama earthquakes, similar to the mechanism that generates slow-slip events [Bürgmann, 2018]. Any pre-existing stresses could have driven more deformation than would be predicted by a model in which only coseismic stress changes are considered, and could have led to increased reloading of the rupture area. The kinematic forward models in Figure 11c demonstrate that any shallow triggered slip caused by the relaxation of pre-existing stresses would generate extension in triangles that span the fault and contraction within the fault hangingwall. Deep slip, on the other hand, would generate mostly extensional strain within the fault hangingwall (Figure 11d). The GPS measurements of inter-event strain can therefore be used to constrain the amplitude of deep and shallow triggered slip, and the associated shear stress recovery.

We performed a grid search of models in which we imposed slip around the edge of the coseismic rupture on the shallow (<5 km) and deep (5–10 km) sections of the Mochiyama Fault, and evaluated the fit between the models and the strain observations (Figure 12). We found that the amplitude of shallow triggered slip is limited to 60–90 cm in order to account for the amplitude of the across-fault fault extension during the inter-event period. For this amount of shallow slip, there cannot have been more than 30–40 cm of triggered slip or localised viscous shear beneath the coseismic rupture, as this would produce extensional strain within the fault hangingwall that is not consisted with the observed strain. These constraints on the amount of shallow and deep triggered slip limit the shear stress recovery that could have been caused by the relaxation of pre-existing stresses to 50–80% of the coseismic stress drop (3–10 MPa; Figure 12).

4 Discussion

4.1 Surface Strain and Stress Changes on the Mochiyama Fault

Our modelling demonstrates that postseismic relaxation driven by coseismic stress changes can account for the pattern and amplitude of the strain observed across the Mochiyama Fault if the stress drop in the earthquake was at least 10 MPa and all of the coseismic stress changes were relaxed by creep and viscous flow in the inter-event period. As the stress changes on the rupture area of the Mochiyama Fault caused by postseismic relaxation are proportional to the coseismic stress drop, however, a higher stress drop does not equate to a higher shear stress recovery. Models that only include the relaxation of the coseismic stress changes in the 2011 Mochiyama earthquake, and that match the observed inter-event strain, recover only 35% of the fault-averaged coseismic shear stress drop, or less.

Although these models can account for the amplitude of the observed deformation, they cannot account for a number of other observations from the Ibaraki-Fukushima earthquake sequence. Firstly, such a stress drop would require average differential stresses within the top 10 km of the crust of at least 20 MPa. It is unlikely the differential stresses exceed a few tens of MPa, given the widespread change in the mechanisms of earthquakes in mainland Japan following the relatively minor (<1–2 MPa) stress changes caused by the Tohoku-oki earthquake [Wang et al., 2019]. Secondly, the assumption that all of the coseismic stress change imposed on the mid-lower crust was relaxed over the 6 year inter-event period would require an effective viscosity of $\lesssim 10^{18}$ Pa s at 10–40 km depth. Such effective viscosities are far lower than those derived from matching geodetic measurements of the response of the crust to stress changes in large megathrust earthquakes ($\sim 10^{19}$–10^{21} Pa s; see Thatcher et al. [1980]; Muto et al. [2019]). Incomplete relaxation of the coseismic stress changes through viscous flow in the mid-lower crust would lead to less reloading than our estimates (i.e. <40% of the coseismic stress drop of 3–10 MPa). Finally, relaxation of only coseismic stress changes cannot account for the order-of-magnitude difference in the amplitude of the deformation observed following 2011 and 2016 earthquakes, suggesting some other stress contribution is needed to explain this feature of the postseismic deformation around the Mochiyama Fault.

The static stress changes due to the nearby Iwaki earthquakes moved the Mochiyama Fault closer to failure, but recovered only <10% of the stress drop in the 2011 Mochiyama earthquake. Subsequent postseismic relaxation will have unloaded the Mochiyama Fault and moved it further from failure. Therefore the stress changes caused by the nearby Iwaki earthquake sequence had a small effect on reloading the Mochiyama Fault in comparison to the localised postseismic relaxation around the margins of the coseismic rupture, and cannot account for the differences between the postseismic deformation after the 2011 and 2016 Mochiyama earthquakes.

The Tohoku-oki earthquake, and its postseismic deformation, could have increased the amount of afterslip on the Mochiyama Fault and brought the rupture area closer to failure. Models that include these effects can account for the amplitude of the measured across-fault extension in the inter-event period and the order-of-magnitude difference in the amplitude of the across-fault extension observed following the 2011 and 2016 Mochiyama earthquakes. However, the inference of Fukushima et al. [2018] that this additional afterslip on the Mochiyama Fault reloaded it back to its former failure stress is inconsistent with our model results. We instead find that the rupture area on the Mochiyama Fault could only have been reloaded by less than half of the coseismic shear stress drop by the time of the 2016 earthquake.

Alternatively, over the inter-event period (2011–2016), there may have been some triggered slip around the rupture area on the Mochiyama Fault that relaxed pre-existing stresses. The GPS data cannot differentiate between coseismic stress-driven afterslip, or triggered slip that does not correlate with coseismic stress changes. Nevertheless, we find that triggered slip cannot have led to a shear stress recovery larger than 50–80% of the coseismic shear stress drop, and again would not have been able to entirely reload the rupture on the Mochiyama Fault. This mechanism also seems unlikely, given that it needs enough elastic strain to have been stored around the margins of the rupture area to generate nearly twice as much postseismic slip than there was coseismic slip in the 2011 Mochiyama earthquake. We therefore conclude that the stresses needed to break the fault in earthquakes must have decreased through time to account for the short inter-event time between the 2011 and 2016 Mochiyama earthquakes by at least 1–5 MPa (50–80% of the stress drop; Figure 13).

4.2 Time-Dependent Decrease in Fault Strength

Most active faults do not experience such short inter-event times between moderate-magnitude earthquakes, suggesting that the mechanisms that decreased the strength and changed the stresses on the Mochiyama Fault between 2011 and 2016 were unusual. The static strength of a fault's surface can be described by the effective frictional resistance to slip $\mu' = \mu(1 - \lambda)$, where μ is the intrinsic friction and $\lambda = P_f/\sigma$ where P_f is the pore-fluid pressure on the fault [Hubbert and Rubey, 1959]. The drop in fault strength may therefore have been due to a decrease in the intrinsic friction of the material making up the fault surface, or an increase in the pore-fluid pressure within the fault core.

One possibility is that the fault strength decreased immediately following the 2011 Mochiyama earthquake as a result of the frictional slip weakening commonly observed in laboratory experiments [e.g. Dieterich, 1979; Ikari et al., 2013] and failed to recover back to its former level. In this situation, it may have been the unusually fast reloading of the Mochiyama Fault relative to the slow rate of strength recovery that led to the unusually short inter-event time. The high rate of stress recovery was most likely a result of enhanced postseismic deformation around the Mochiyama Fault that relaxed the co- and post-seismic stress changes following the 2011 Mochiyama and Tohoku-oki earthquakes.

Alternatively, the fault may have experienced a more steady decrease in strength. Vertical migration of high-pressure fluids through the shallow crust in mainland Japan following the Tohoku-oki earthquake has been widely invoked to account for migrating seismicity [Yoshida et al., 2015, 2017, 2020], temporal changes in the shallow shear-wave velocity structure [Wang et al., 2021] and groundwater geochemistry around crustal faults [Sato et al., 2020]. Infiltration of fluid onto the rupture area of the Mochiyama Fault could have reduced the average shear stresses needed for failure, whilst also promoting aftershock seismicity, by changing the effective fault-normal stresses [Hainzl, 2004]. We did not find any evidence for the spatial migration of earthquake hypocentres around the Mochiyama Fault that might reflect a fluid front causing small patches of the fault to fail sequentially (Supplementary Figure 13) [e.g. Shapiro et al., 1997; Walters et al., 2018]. Any fluid infiltration onto the fault zone also did not affect the time-scale over which coseismic stress changes were relaxed, as the postseismic transients after the 2011 and 2016 Mochiyama earthquakes followed similar temporal decays. Therefore the mechanism(s) that decreased the strength of the Mochiyama Fault had surprisingly little effect on the geodetic or microseismic observations during the inter-event period, other than the highly energetic aftershock sequence beneath the mainshock rupture area (see Section 2.4).

5 Conclusion

We have demonstrated that earthquake-related stress changes and their postseismic relaxation can explain the pattern of strain measured by Japan's GPS network during the 2011–2016 Mochiyama earthquakes in the Ibaraki-Fukushima region. Models that match the observed inter-event strain can only reload the rupture area on the fault by less than 50–80% of the fault-averaged coseismic stress drop (3–10 MPa), irrespective of the rheological structure of the crust and mantle, or the mechanisms of postseismic relaxation. We conclude that the Mochiyama Fault experienced a drop in its effective strength, and the shear stresses needed to break the fault reduced by at least 1–5 MPa. The mechanism(s) that caused this weakening are unclear, but appear to have been associated with an unusually energetic aftershock sequence around the margins of the coseismic rupture. Time-dependent changes in fault strength may therefore play a role in modulating the timing of moderate-magnitude earthquakes, but may be difficult to detect using geodetic and microseismicity observations.

Acknowledgements

SW was supported by the Denman Baynes Junior Research Fellowship at Clare College, University of Cambridge. Part of this work was completed during NF's M.Sci thesis at the University of Cambridge. This work was partly supported by COMET – the NERC Centre for the Observation and Modelling of Earthquakes, Volcanoes, and Tectonics, a partnership between UK universities and the BGS. Both SW and NF contributed equally to this article. The authors thank Dr. Yo Fukushima, Dr. Takahiko Uchide, Dr. Keitaro Komura and Dr. Yan Hu for swiftly providing data from their publications. The authors also thank the Associate Editor Dr. Eiichi Fukuyama, one anonymous reviewer and Prof. Roland Burgmann for their constructive reviews.

Data Availability

All data and code used in this study are freely available online. The GPS data used in this study are available from `https://www.gsi.go.jp/ENGLISH/geonet_english.html` (last accessed July 2022). The JMA microseismicity data are available from `https://www.data.jma.go.jp/svd/eqev/data/bulletin/index_e.html` (last accessed March 2021) and the NIED earthquake moment tensors are available from `https://www.fnet.bosai.go.jp/fnet/event/search.php` (last accessed March 2021). The Envisat and Sentinel-1 data are freely accessible through ESAs Copernicus Schihub `https://scihub.copernicus.eu/` (last accessed January 2022). The numerical model RELAX is available from `https://geodynamics.org/cig/software/relax/` (last accessed March 2021).

References

Bagge, M. and Hampel, A. (2017). Postseismic Coulomb stress changes on intra-continental dip-slip faults due to viscoelastic relaxation in the lower crust and lithospheric mantle: insights from 3D finite-element modelling. *International Journal of Earth Sciences*, 106(8):2895–2914.

Barbot, S. and Fialko, Y. (2010a). A unified continuum representation of post-seismic relaxation mechanisms: semi-analytic models of afterslip, poroelastic rebound and viscoelastic flow. *Geophysical Journal International*, 182(3):1124–1140.

Barbot, S. and Fialko, Y. (2010b). Fourier-domain Green's function for an elastic semi-infinite solid under gravity, with applications to earthquake and volcano deformation. *Geophysical Journal International*, 182(2):568–582.

Barbot, S., Fialko, Y., and Bock, Y. (2009). Postseismic deformation due to the Mw 6.0 2004 Parkfield earthquake: Stress-driven creep on a fault with spatially variable rate-and-state friction parameters. *Journal of Geophysical Research: Solid Earth*, 114(B7):B07405.

Becker, T. W., Hashima, A., Freed, A. M., and Sato, H. (2018). Stress change before and after the 2011 M9 Tohoku-oki earthquake. *Earth and Planetary Science Letters*, 504:174–184.

Bedford, J. R., Moreno, M., Deng, Z., Oncken, O., Schurr, B., John, T., Báez, J. C., and Bevis, M. (2020). Months-long thousand-kilometre-scale wobbling before great subduction earthquakes. *Nature*, 580(7805):628–635.

Bourne, S. J., Árnadóttir, T., Beavan, J., Darby, D. J., England, P. C., Parsons, B., Walcott, R. I., and Wood, P. R. (1998). Crustal deformation of the Marlborough Fault Zone in the South Island of New Zealand: Geodetic constraints over the interval 1982-1994. *Journal of Geophysical Research: Solid Earth*, 103(B12):30147–30165.

Bürgmann, R. (2018). The geophysics, geology and mechanics of slow fault slip. *Earth and Planetary Science Letters*, 495:112–134.

Byerlee, J. (1978). Friction of rocks. *Pure and Applied Geophysics*, 116(4-5):615–626.

Cheloni, D., D'Agostino, N., D'Anastasio, E., Avallone, A., Mantenuto, S., Giuliani, R., Mattone, M., Calcaterra, S., Gambino, P., Dominici, D., Radicioni, F., and Fastellini, G. (2010). Coseismic and initial post-seismic slip of the 2009 Mw 6.3 L'Aquila earthquake, Italy, from GPS measurements. *Geophysical Journal International*, 181(3):1539–1546.

Christensen, D. H. and Ruff, L. J. (1985). Analysis of the trade-off between hypocentral depth and source time function. *Bulletin of the Seismological Society of America*, 75(6):1637–1656.

Churchill, R. M., Werner, M. J., Biggs, J., and Fagereng, Å. (2022). Afterslip Moment Scaling and Variability From a Global Compilation of Estimates. *Journal of Geophysical Research: Solid Earth*, 127(4):e2021JB023897.

Collettini, C., Tesei, T., Scuderi, M. M., Carpenter, B. M., and Viti, C. (2019). Beyond Byerlee friction, weak faults and implications for slip behavior. *Earth and Planetary Science Letters*, 519:245–263.

Copley, A. (2018). The strength of earthquake-generating faults. *Journal of the Geological Society*, 174(1).

Dieterich, J. H. (1979). Modeling of rock friction 1. Experimental results and constitutive equations. *Journal of Geophysical Research: Solid Earth*, 84(B5):2161–2168.

Dziewonski, A. M., Chou, T.-A., and Woodhouse, J. H. (1981). Determination of earthquake source parameters from waveform data for studies of global and regional seismicity. *Journal of Geophysical Research: Solid Earth*, 86(B4):2825–2852.

Ekström, G., Nettles, M., and Dziewoński, A. (2012). The global CMT project 20042010: Centroid-moment tensors for 13,017 earthquakes. *Physics of the Earth and Planetary Interiors*, 200:1–9.

Ellis, S. and Stöckhert, B. (2004). Elevated stresses and creep rates beneath the brittle-ductile transition caused by seismic faulting in the upper crust. *Journal of Geophysical Research: Solid Earth*, 109(5).

Farr, T. G., Rosen, P. A., Caro, E., Crippen, R., Duren, R., Hensley, S., Kobrick, M., Paller, M., Rodriguez, E., Roth, L., Seal, D., Shaffer, S., Shimada, J., Umland, J., Werner, M., Oskin, M., Burbank, D., and Alsdorf, D. (2007). The Shuttle Radar Topography Mission. *Reviews of Geophysics*, 45(2):RG2004.

Freed, A. M. (2005). Earthquake Triggering by Static, Dynamic and Postseismic Stress Transfer. *Annual Review of Earth and Planetary Sciences*, 33(1):335–367.

Freed, A. M. and Lin, J. (1998). Time-dependent changes in failure stress following thrust earthquakes. *Journal of Geophysical Research: Solid Earth*, 103(10):24393–24409.

Fukushima, Y., Takada, Y., and Hashimoto, M. (2013). Complex ruptures of the 11 April 2011 Mw 6.6 Iwaki earthquake triggered by the 11 march 2011 Mw 9.0 Tohoku earthquake, Japan. *Bulletin of the Seismological Society of America*, 103(2 B):1572–1583.

Fukushima, Y., Toda, S., Miura, S., Ishimura, D., Fukuda, J., Demachi, T., and Tachibana, K. (2018). Extremely early recurrence of intraplate fault rupture following the Tohoku-Oki earthquake. *Nature Geoscience*, 11(10):777–781.

Hainzl, S. (2004). Seismicity patterns of earthquake swarms due to fluid intrusion and stress triggering. *Geophysical Journal International*, 159(3):1090–1096.

Hayes, G. P. (2017). The finite, kinematic rupture properties of great-sized earthquakes since 1990. *Earth and Planetary Science Letters*, 468(June 2016):94–100.

Hu, Y., Bürgmann, R., Uchida, N., Banerjee, P., and Freymueller, J. T. (2016). Stress-driven relaxation of heterogeneous upper mantle and time-dependent afterslip following the 2011 Tohoku earthquake. *Journal of Geophysical Research: Solid Earth*, 121(1):385–411.

Hubbert, M. K. and Rubey, W. W. (1959). Mechanics of fluid-filled porous solids and its application to overthrust faulting. *Bulletin of the Geological Society of America*, 70(2):115–166.

Ikari, M. J., Marone, C., Saffer, D. M., and Kopf, A. J. (2013). Slip weakening as a mechanism for slow earthquakes. *Nature Geoscience*, 6(6):468–472.

Imanishi, K., Ando, R., and Kuwahara, Y. (2012). Unusual shallow normal-faulting earthquake sequence in compressional northeast Japan activated after the 2011 off the Pacific coast of Tohoku earthquake. *Geophysical Research Letters*, 39(9).

Kagan, Y. Y., Jackson, D. D., and Geller, R. J. (2012). Characteristic earthquake model, 1884-2011, R.I.P.

Kato, A., Sakai, S., and Obara, K. (2011). A normal-faulting seismic sequence triggered by the 2011 off the Pacific coast of Tohoku Earthquake: Wholesale stress regime changes in the upper plate. *Earth, Planets and Space*, 63(7):745–748.

King, G. C. P., Stein, R. S., and Lin, J. (1994). Static stress changes and the triggering of earthquakes. *Bulletin of the Seismological Society of America*, 84(3):935–953.

Komura, K., Aiyama, K., Nagata, T., Sato, H. P., Yamada, A., and Aoyagi, Y. (2019). Surface rupture and characteristics of a fault associated with the 2011 and 2016 earthquakes in the southern Abukuma Mountains, northeastern Japan, triggered by the Tohoku-Oki earthquake. *Earth, Planets and Space*, 71(1):1–23.

McCaffrey, R. and Abers, G. (1988). Syn3: a program for inversion of teleseismic body waveforms on microcomputers.

Murray, J. and Segall, P. (2002). Testing time-predictable earthquake recurrence by direct measurement of strain accumulation and release. *Nature*, 419(6904):287–291.

Muto, J., Moore, J. D., Barbot, S., Iinuma, T., Ohta, Y., and Iwamori, H. (2019). Coupled afterslip and transient mantle flow after the 2011 Tohoku earthquake. *Science Advances*, 5(9).

Nabalek, J. (1984). *Determination of earthquake source parameters from inversion of body waves.* PhD thesis, Massachusetts Institute of Technology.

Okada, T., Yoshida, K., Ueki, S., Nakajima, J., Uchida, N., Matsuzawa, T., Umino, N., and Hasegawa, A. (2011). Shallow inland earthquakes in NE Japan possibly triggered by the 2011 off the Pacific coast of Tohoku Earthquake. *Earth, Planets and Space*, 63(7):749–754.

Okada, Y. (1992). Internal deformation due to shear and tensile faults in a half-space. *Bulletin of the Seismological Society of America*, 82(2):1018–1040.

Ozawa, S., Nishimura, T., Suito, H., Kobayashi, T., Tobita, M., and Imakiire, T. (2011). Coseismic and postseismic slip of the 2011 magnitude-9 Tohoku-Oki earthquake. *Nature*, 475(7356):373–376.

Reid, H. F. (1910). The Mechanics of the Earthquake, The California Earthquake of April 18, 1906. Technical report, Carnegie Institution of Washington, Washington D.C.

Roeloffs, E. and Langbein, J. (1994). The Earthquake Prediction Experiment at Parkfield, California.

Sato, T., Kazahaya, K., Matsumoto, N., and Takahashi, M. (2020). Deep groundwater discharge after the 2011 Mw 6.6 Iwaki earthquake, Japan. *Earth, Planets and Space*, 72(1).

Shapiro, S. A., Huenges, E., and Borm, G. (1997). Estimating the crust permeability from fluid-injection-induced seismic emission at the KTB site. *Geophysical Journal International*, 131(2):5–8.

Sieh, K., Natawidjaja, D. H., Meltzner, A. J., Shen, C. C., Cheng, H., Li, K. S., Suwargadi, B. W., Galetzka, J., Philibosian, B., and Edwards, R. L. (2008). Earthquake supercycles inferred from sea-level changes recorded in the corals of west Sumatra. *Science*, 322(5908):1674–1678.

Taymaz, T., Jackson, J. A., and Westaway, R. (1990). Earthquake mechanisms in the Hellenic Trench near Crete. *Geophysical Journal International*, 102(3):695–731.

Thatcher, W., Matsuda, T., Kato, T., and Rundle, J. B. (1980). Lithospheric loading by the 1896 Riku-u earthquake, northern Japan: implications for plate flexure and asthenospheric rheology. *Journal of Geophysical Research*, 85(B11):6429–6435.

Toda, S., Stein, R. S., Sevilgen, V., and Lin, J. (2011). Coulomb 3.3 Graphic-rich deformation and stress-change software for earthquake, tectonic, and volcano research and teaching-user guide. *Open-File Report*.

Toda, S. and Tsutsumi, H. (2013). Simultaneous reactivation of two, subparallel, inland normal faults during the Mw 6.6 11 April 2011 Iwaki earthquake triggered by the Mw 9.0 Tohoku-oki, Japan, Earthquake. *Bulletin of the Seismological Society of America*, 103(2 B):1584–1602.

Twardzik, C., Vergnolle, M., Sladen, A., and Avallone, A. (2019). Unravelling the contribution of early postseismic deformation using sub-daily GNSS positioning. *Scientific Reports*, 9(1):1775.

Uchide, T. and Imanishi, K. (2018). Underestimation of Microearthquake Size by the Magnitude Scale of the Japan Meteorological Agency: Influence on Earthquake Statistics. *Journal of Geophysical Research: Solid Earth*, 123(1):606–620.

Virtanen, P., Gommers, R., Oliphant, T. E., Haberland, M., Reddy, T., Cournapeau, D., Burovski, E., Peterson, P., Weckesser, W., Bright, J., van der Walt, S. J., Brett, M., Wilson, J., Millman, K. J., Mayorov, N., Nelson, A. R., Jones, E., Kern, R., Larson, E., Carey, C. J., Polat, ., Feng, Y., Moore, E. W., VanderPlas, J., Laxalde, D., Perktold, J., Cimrman, R., Henriksen, I., Quintero, E. A., Harris, C. R., Archibald, A. M., Ribeiro, A. H., Pedregosa, F., van Mulbregt, P., Vijaykumar, A., Bardelli, A. P., Rothberg, A., Hilboll, A., Kloeckner, A., Scopatz, A., Lee, A., Rokem, A., Woods, C. N., Fulton, C., Masson, C., Häggström, C., Fitzgerald, C., Nicholson, D. A., Hagen, D. R., Pasechnik, D. V., Olivetti, E., Martin, E., Wieser, E., Silva, F., Lenders, F., Wilhelm, F., Young, G., Price, G. A., Ingold, G. L., Allen, G. E., Lee, G. R., Audren, H., Probst, I., Dietrich, J. P., Silterra, J., Webber, J. T., Slavič, J., Nothman, J., Buchner, J., Kulick, J., Schönberger, J. L., de Miranda Cardoso, J. V., Reimer, J., Harrington, J., Rodríguez, J. L. C., Nunez-Iglesias, J., Kuczynski, J., Tritz, K., Thoma, M., Newville, M., Kümmerer, M., Bolingbroke, M., Tartre, M., Pak, M., Smith, N. J., Nowaczyk, N., Shebanov, N., Pavlyk, O., Brodtkorb, P. A., Lee, P., McGibbon, R. T., Feldbauer, R., Lewis, S., Tygier, S., Sievert, S., Vigna, S., Peterson, S., More, S., Pudlik, T., Oshima, T., Pingel, T. J., Robitaille, T. P., Spura, T., Jones, T. R., Cera, T., Leslie, T., Zito, T., Krauss, T., Upadhyay, U., Halchenko, Y. O., and Vázquez-Baeza, Y. (2020). SciPy 1.0: fundamental algorithms for scientific computing in Python. *Nature Methods*, 17(3):261–272.

Waldhauser, F. and Ellsworth, W. L. (2000). A Double-difference Earthquake location algorithm: Method and application to the Northern Hayward Fault, California. *Bulletin of the Seismological Society of America*, 90(6):1353–1368.

Walters, R. J., Gregory, L. C., Wedmore, L. N., Craig, T. J., McCaffrey, K., Wilkinson, M., Chen, J., Li, Z., Elliott, J. R., Goodall, H., Iezzi, F., Livio, F., Michetti, A. M., Roberts, G., and Vittori, E. (2018). Dual control of fault intersections on stop-start rupture in the 2016 Central Italy seismic sequence. *Earth and Planetary Science Letters*, 500:1–14.

Wang, K., Zhu, Y., Nissen, E., and Shen, Z. K. (2021). On the Relevance of Geodetic Deformation Rates to Earthquake Potential. *Geophysical Research Letters*, 48(11):e2021GL093231.

Wang, S., Xu, W., Xu, C., Yin, Z., Bürgmann, R., Liu, L., and Jiang, G. (2019). Changes in groundwater level possibly encourage shallow earthquakes in central Australia: The 2016 Petermann Ranges earthquake. *Geophysical Research Letters*, 46(6):3189–3198.

Wdowinski, S., Bock, Y., Zhang, J., Fang, P., and Genrich, J. (1997). Southern California Permanent GPS Geodetic Array: Spatial filtering of daily positions for estimating coseismic and postseismic displacements induced by the 1992 Landers earthquake. *Journal of Geophysical Research: Solid Earth*, 102(B8):18057–18070.

Yoshida, K., Hasegawa, A., and Okada, T. (2015). Spatially heterogeneous stress field in the source area of the 2011 Mw 6.6 Fukushima-Hamadori earthquake, NE Japan, probably caused by static stress change. *Geophysical Journal International*, 201(2):1062–1071.

Yoshida, K., Saito, T., Urata, Y., Asano, Y., and Hasegawa, A. (2017). Temporal Changes in Stress Drop, Frictional Strength, and Earthquake Size Distribution in the 2011 Yamagata-Fukushima, NE Japan, Earthquake Swarm, Caused by Fluid Migration. *Journal of Geophysical Research: Solid Earth*, 122(12):10,379–10,397.

Yoshida, K., Uchida, N., Hiarahara, S., Nakayama, T., Matsuzawa, T., Okada, T., Matsumoto, Y., and Hasegawa, A. (2020). 2019 M6.7 Yamagata-Oki earthquake in the stress shadow of 2011 Tohoku-Oki earthquake: Was it caused by the reduction in fault strength? *Tectonophysics*, 793(August):228609.

Zakharova, O., Hainzl, S., and Bach, C. (2013). Seismic moment ratio of aftershocks with respect to main shocks. *Journal of Geophysical Research: Solid Earth*, 118(11):5856–5864.

Zebker, H. A. and Lu, Y. (1998). Phase unwrapping algorithms for radar interferometry: residue-cut, least-squares, and synthesis algorithms. *Journal of the Optical Society of America A*, 15(3):586.

Zwick, P., McCaffrey, R., and Abers, G. (1994). MT5 Program.

Tables

Table 1: Parameters used in the generalised model calculations in Section 3.1.

Model Parameter	Symbol	Value
Discretisation	Δx_j	0.2 km
Number of nodes	N_j	512
Density	ρ	2800 kg/m^3
First Lamé parameter	λ	30 GPa
Shear modulus	G	30 GPa
Poisson's ratio	ν	0.25
Fault strike	θ	180°
Fault dip	δ	45°
Fault rake	ϕ	-90°

Figures

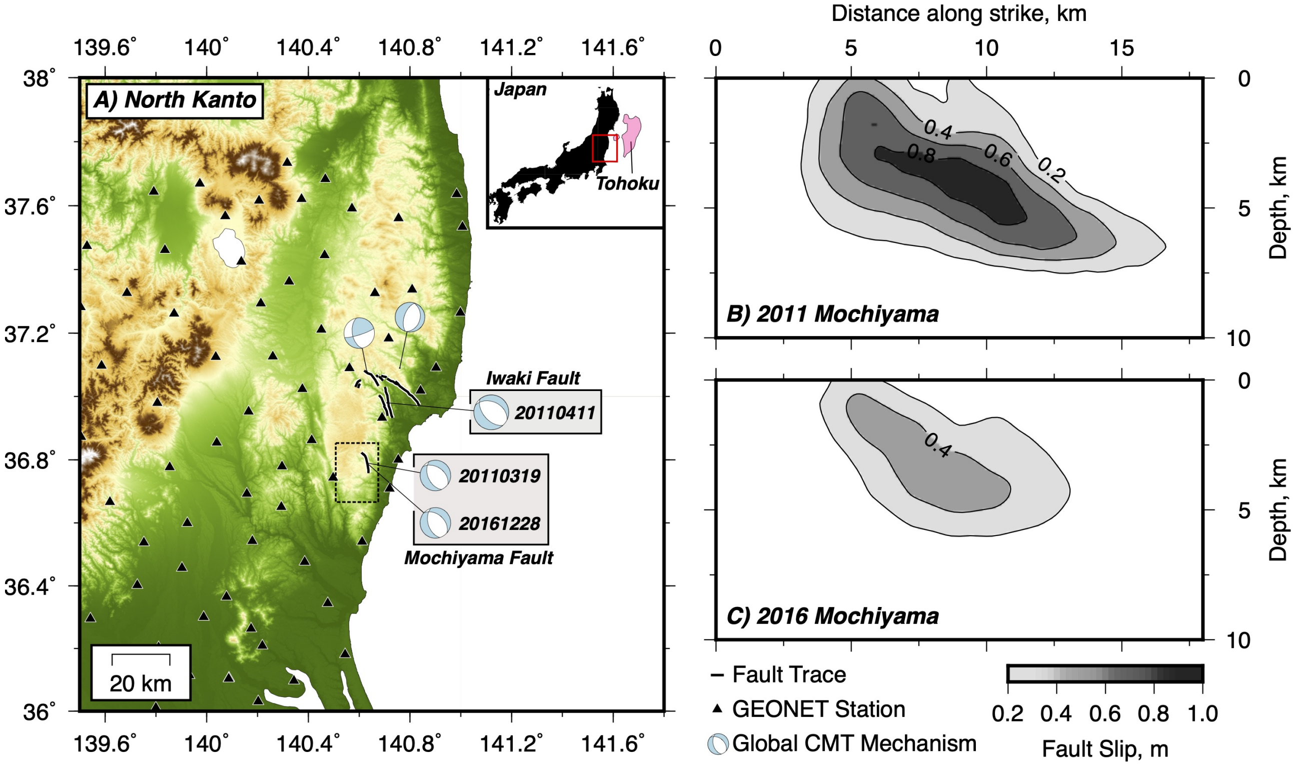

Figure 1: Overview of the Ibaraki-Fukushima earthquake sequence. (a) Map of the study region showing the locations and Global CMT mechanisms of the Mochiyama and Iwaki earthquake sequences [Ekström et al., 2012]. GEONET GPS stations are shown as black triangles and the surface rupture traces from Toda and Tsutsumi [2013] and Komura et al. [2019] as black lines. The dashed black box is the area covered by coseismic and postseismic SAR measurements shown in Figure 4. The inset map shows the location of the study region relative to the 10 m coseismic slip contour in the M_w 9.1 11th March 2011 Tohoku-oki earthquake taken from Hayes [2017]. (b) and (c) show the slip distributions in the 2011 and 2016 Mochiyama earthquakes determined by Fukushima et al. [2018]. The slip distribution in (b) was derived using two ALOS-1 interferograms spanning the dates 2011/02/02–2011/03/20 for the ascending track and 2010/11/20-2011/04/07 for the descending track. The slip distribution in (c) was derived using three ALOS-2 frames spanning 2016/11/15–2017/02/21 and 2016/11/01–2017/02/07 from the ascending track and 2016/11/17–2016/12/29 from the descending track, plus static GPS displacements from the GEONET network.

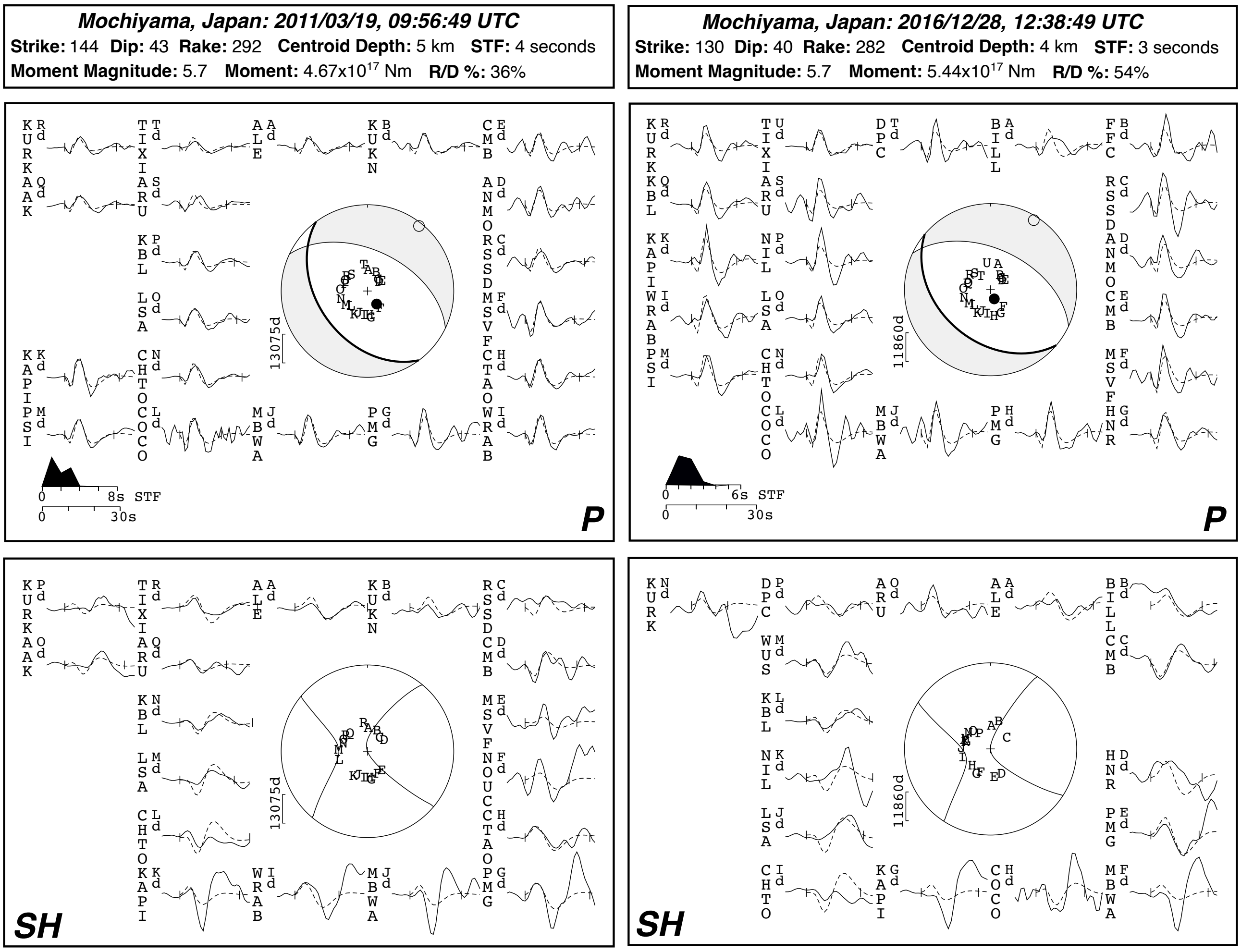

Figure 2: Minimum-misfit body-waveform models for the 2011 and 2016 Mochiyama earthquakes. The minimum-misfit parameters for each model are shown in the top panels, where STF is the source-time function and R/D% is the ratio of the residual variance to the data variance expressed as a percentage. The middle panel shows the fit between the modelled (dashed) and observed (solid) waveforms for the *P* waves. Each seismogram has to its left the three/four-letter station code, and a capital letter that corresponds to the letters plotted on the focal sphere. The source-time function and time-scale for the plotted waveforms is shown in the bottom left. The *SH* waveforms are shown in the bottom panel using the same format.

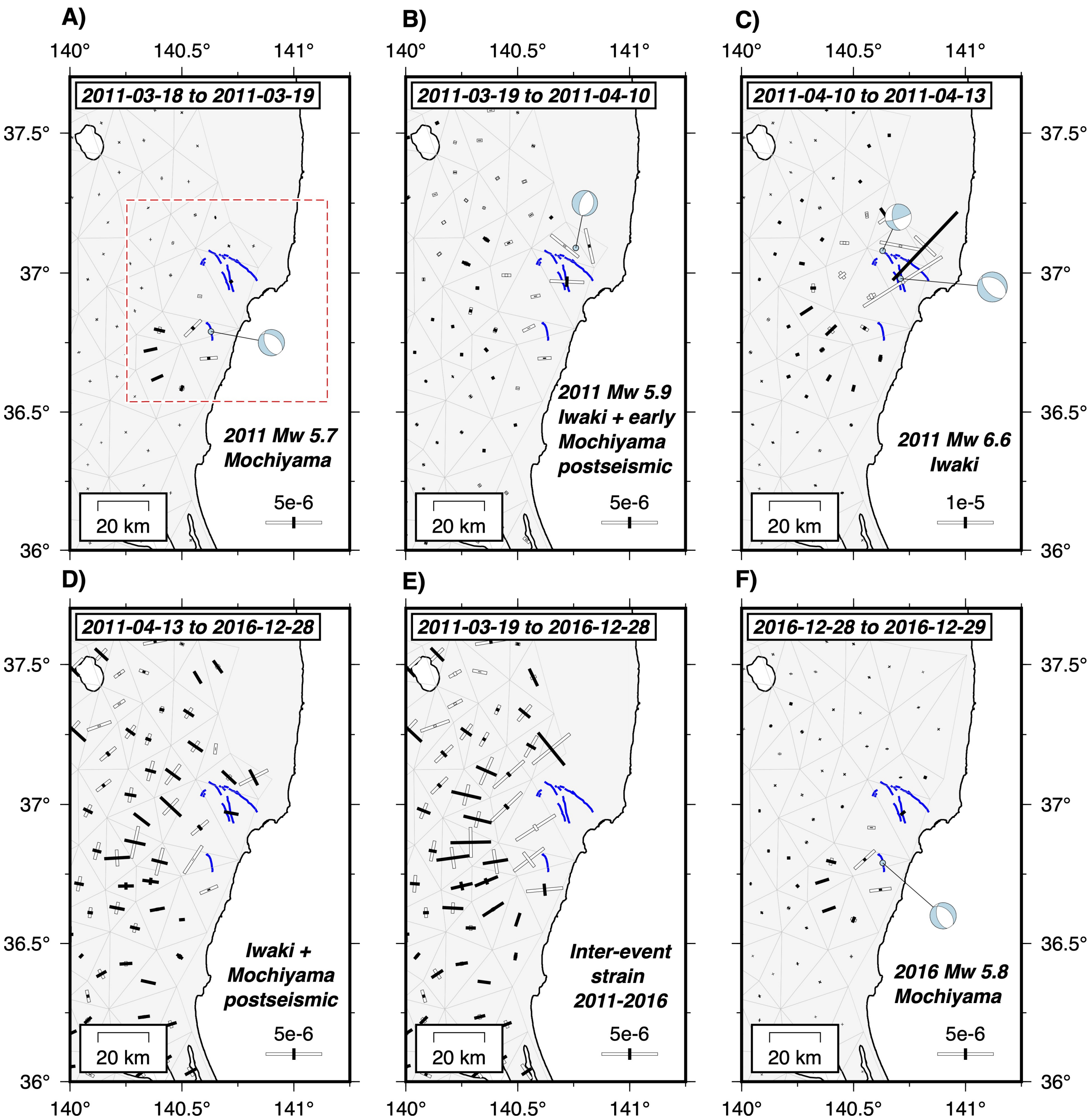

Figure 3: Incremental strain through the 2011-2016 Ibaraki-Fukushima earthquake sequence. White bars represent principal axes of extensional strain, whilst black bars are principal axes of contractional strain. Note the difference in bar scaling between certain epochs. Blue lines are the surface traces of the Mochiyama and Iwaki Faults from Fukushima et al. [2013] and Komura et al. [2019], and the red dashed box in (a) is the map area shown in Figures 5 and 8. The GPS triangles spanning the Iwaki Fault are removed from (e) to highlight the inter-event strain across the Mochiyama Fault.

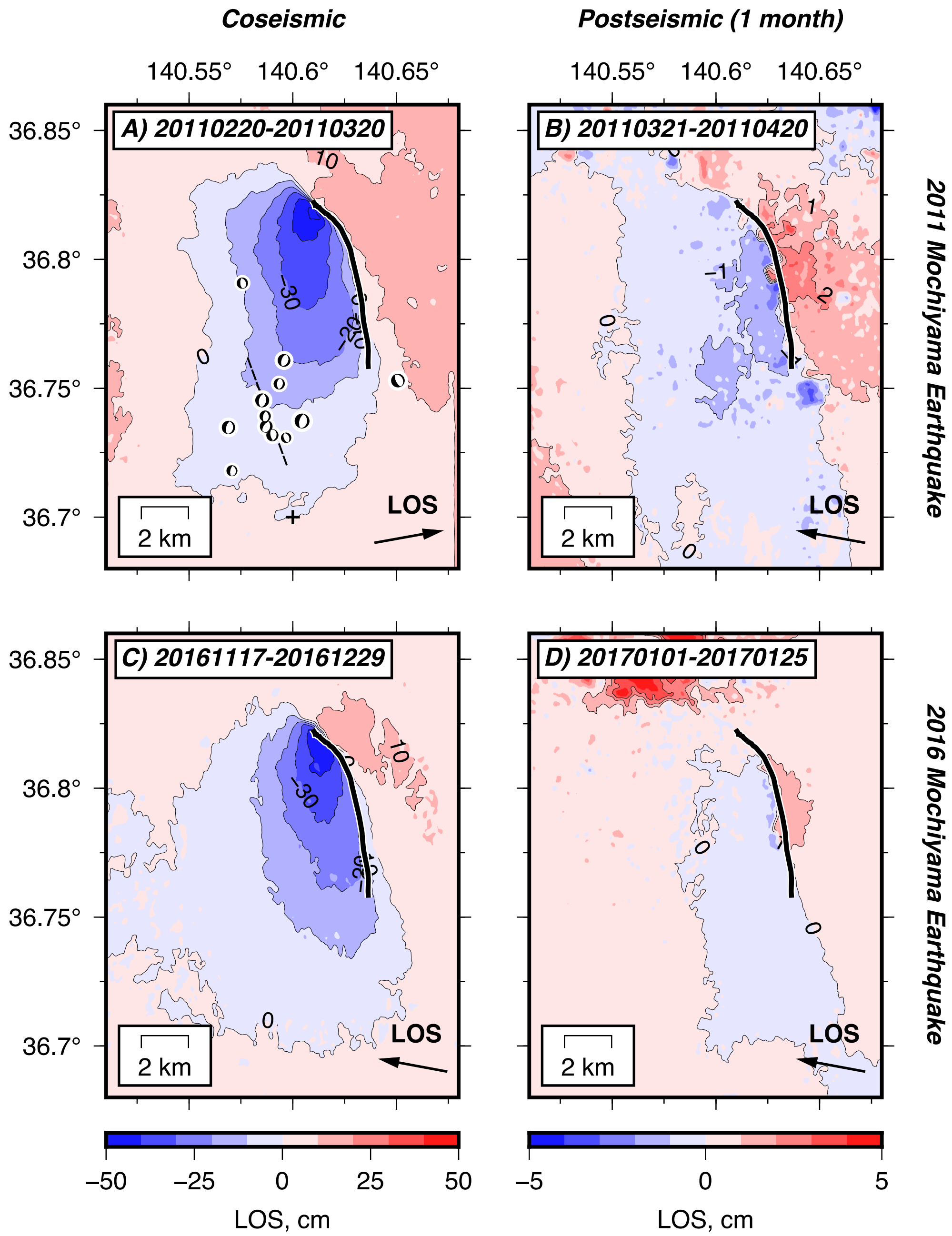

Figure 4: Coseismic and early postseismic interferograms from the 2011 and 2016 earthquakes on the Mochiyama Fault. The surface trace of the fault is shown by the thick black line and the date of the primary and secondary acquisition is shown in the top left in yyymmdd format. Line-of-sight vectors are shown in the bottom right. (a) ALOS-1 ascending track coseismic interferogram showing the LOS displacement in the 19th March 2011 Mochiyama earthquake from Komura et al. [2019]. The interferogram contains 1 day of postseismic deformation. Focal mechanisms are M_w 4 and 5 foreshocks that occurred between the 11th March 2011 and 18th March 2011 from the NIED catalogue. The black-dashed line indicates the strike of the conjugate normal fault seen in the relocated microseismicity (Supplementary Figure 1). (b) Envisat descending track interferogram of the first month of postseismic relaxation after the 2011 earthquake covering the period of 2 to 32 days after the mainshock. (c) ALOS-2 descending track coseismic interferogram covering the 28th December 2016 Mochiyama earthquake from Komura et al. [2019]. The interferogram contains 1 day of postseismic deformation. (d) Sentinel-1 descending track interferogram of the first month of postseismic relaxation after the 2016 earthquake covering the period of 4 to 28 days after the mainshock.

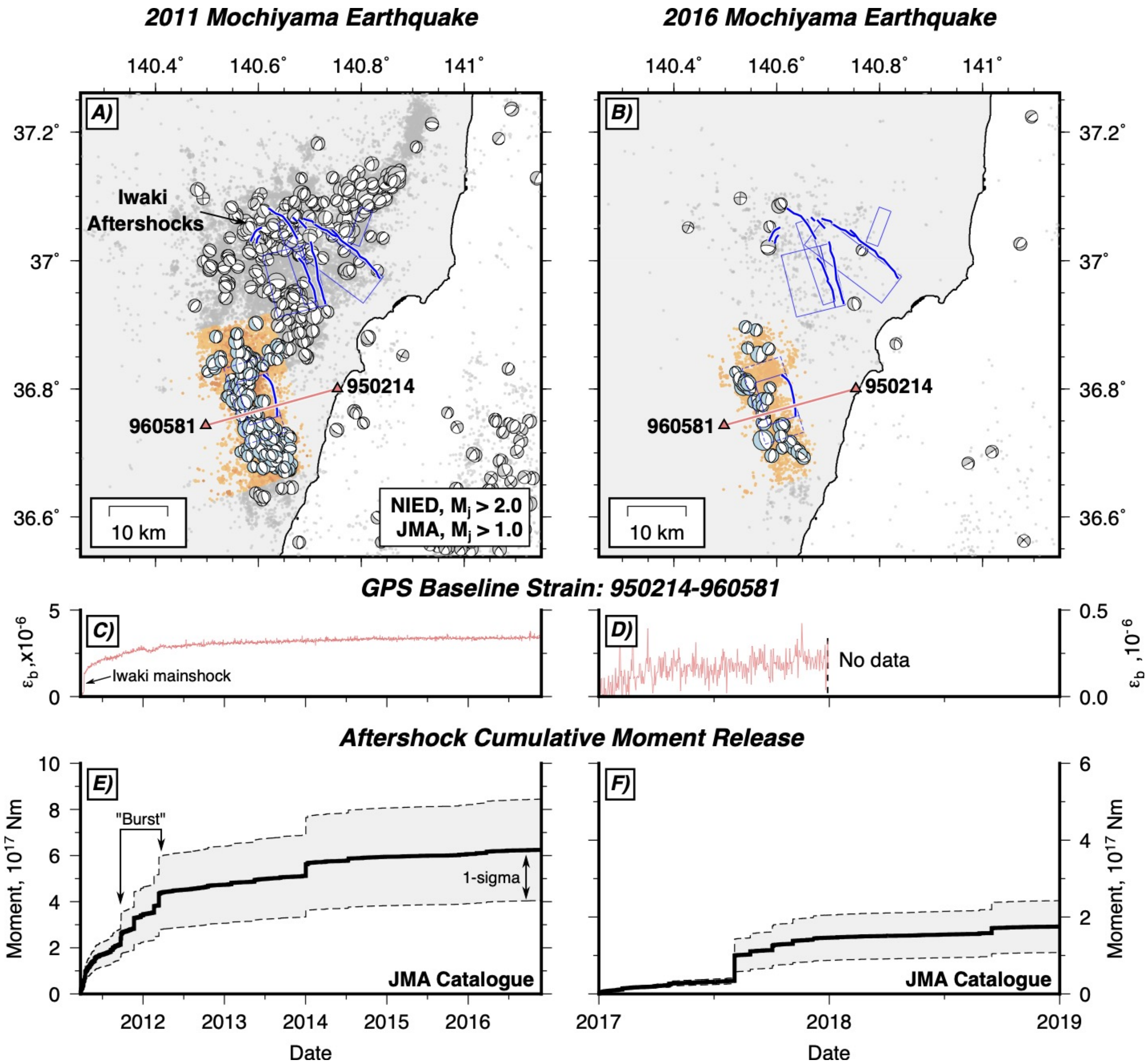

Figure 5: Locations and mechanisms of aftershocks from the JMA unified catalogue and NIED CMT catalogue following the 2011 and 2016 Mochiyama earthquakes. (a) and (b) show the map-view distribution of shallow (<20 km) seismicity relative to the Mochiyama and Iwaki Faults (blue rectangles). Events used in the moment summation in (e) and (f) are shown as gold dots. (c) and (d) show the temporal evolution of baseline strain ε_b between GEONET stations 950214 and 960581 (red triangles in a and b). Note the stark difference in the strain amplitude. (e) and (f) show the temporal evolution of cumulative moment release from aftershocks in the JMA unified catalogue. Uncertainties are shown by the dashed black lines and result from converting local magnitudes M_j to moment magnitudes M_0 using the scaling of Uchide and Imanishi [2018].

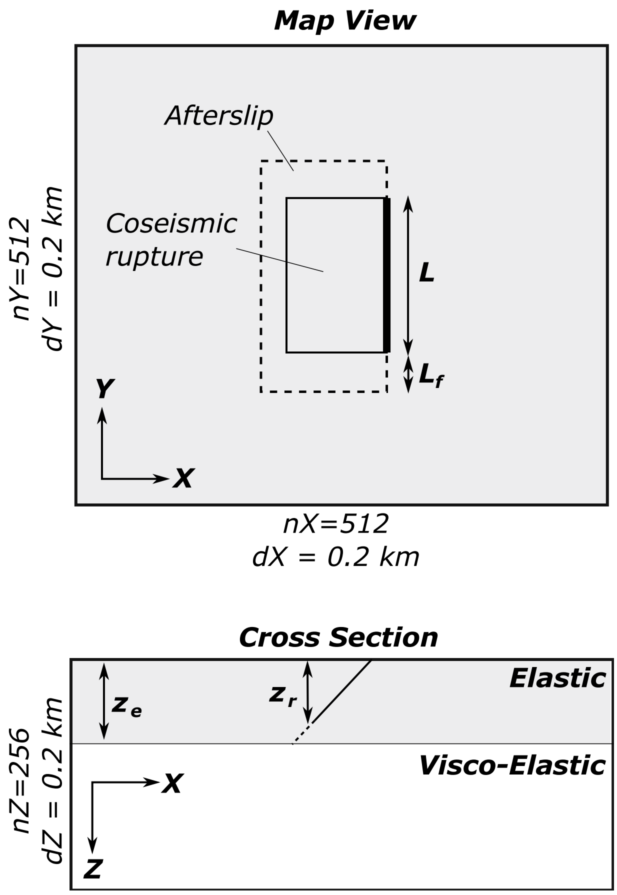

Figure 6: Sketch of the set-up of the generalised numerical calculations in map view (top) and cross-section (bottom). nX, nY and nZ are the number of nodes used in the numerical solutions, and dX, dY and dZ are the spacing between the nodes. The dashed region shows the area of the fault that can slide through postseismic afterslip. The coseismic rupture area is discretised into 8 patches along-strike and 8 patches down-dip.

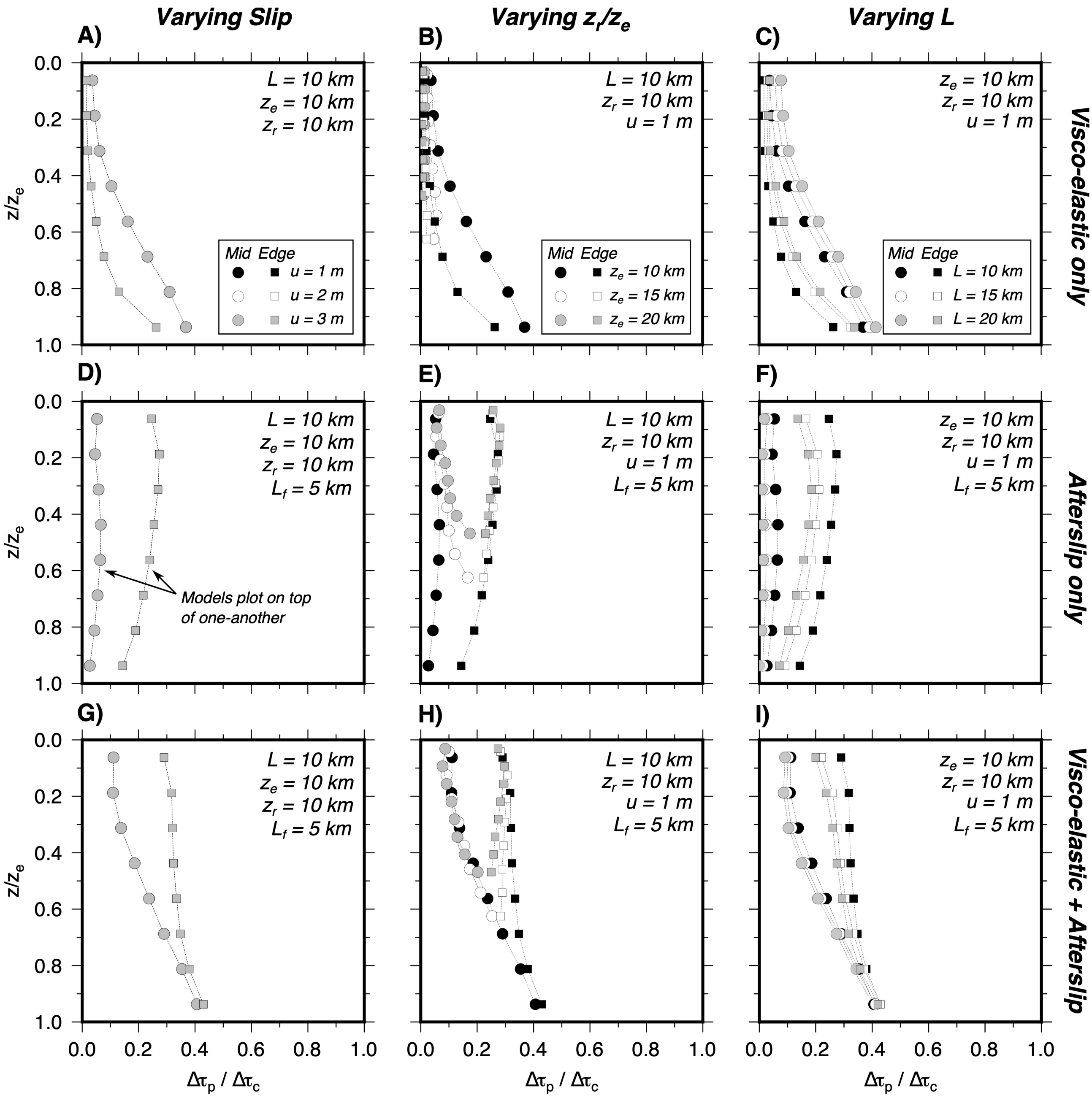

Figure 7: Results of the numerical experiments for the postseismic shear stress recovery $\Delta\tau_p/\Delta\tau_c$ as a function of depth relative to the base of the elastic layer z/z_e when varying the amount of fault slip u (a,d,g), the depth of the fault rupture z_r (b,e,h) and the fault length L (c,f,i). The top row shows models that only include visco-elastic relaxation below $z/z_e > 1$, the middle row shows models that only include frictional afterslip above $z/z_e < 1$, and the bottom row shows models that include both visco-elastic relaxation and afterslip. Circles represent $\Delta\tau_p/\Delta\tau_c$ in the middle of the fault, whilst squares represent $\Delta\tau_p/\Delta\tau_c$ along the lateral edge of the fault. The values of the fixed parameters are shown in the top right of each box.

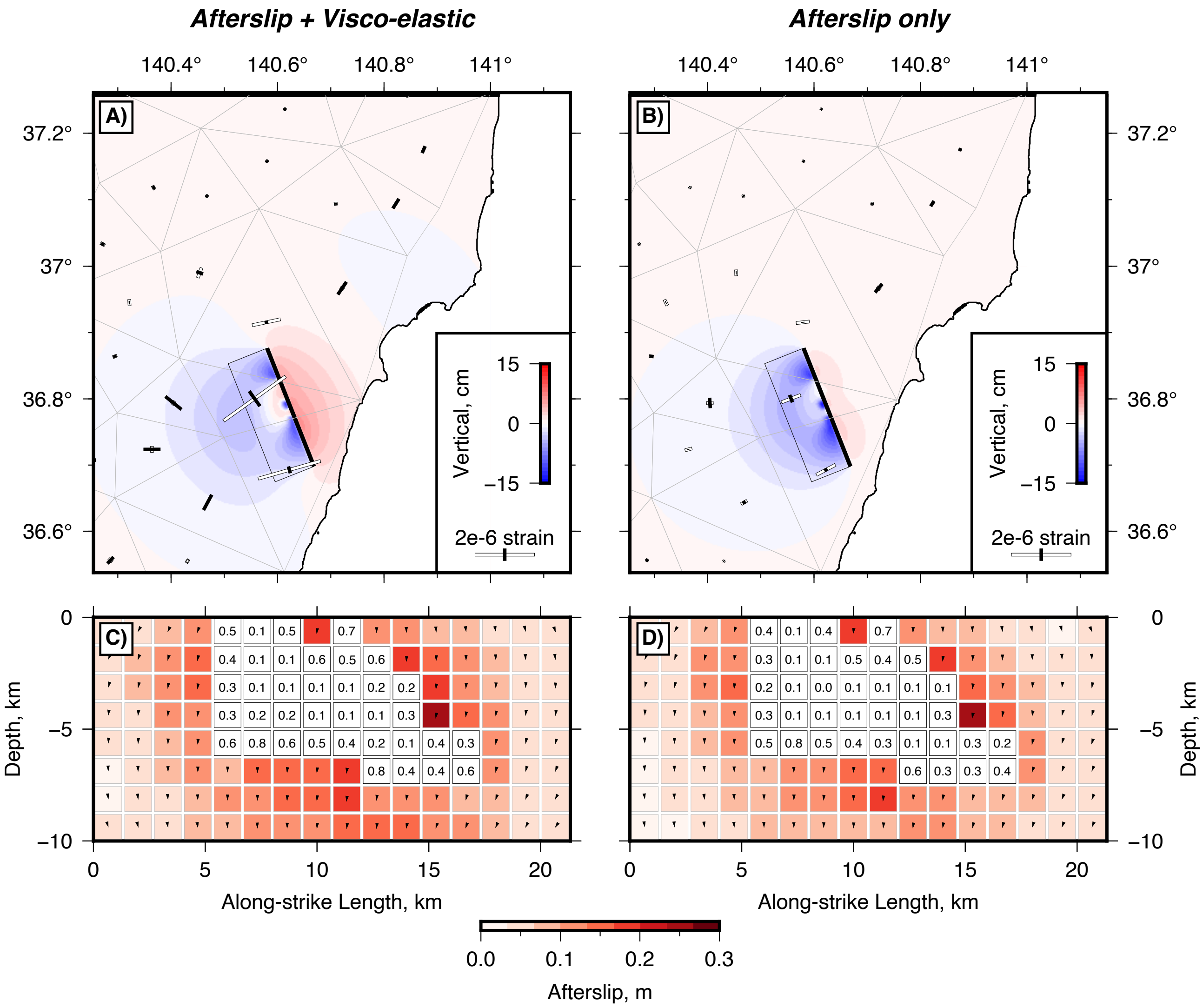

Figure 8: Stress-driven forward models of the postseismic relaxation following the 2011 Mochiyama earthquake. (a) Vertical surface displacements and horizontal strain calculated for a model in which all of the coseismic stress changes are relaxed by afterslip and visco-elastic relaxation. The elastic layer thickness in this calculation is 10 km. (b) The same calculation as in (a), but strain is relaxed by localised shear at depths >10 km and not distributed flow. In (a) and (b) faults are marked by thin black lines, with a thick black line at their up-dip edge. The GPS network is shown by the light grey triangles with GPS stations at their vertices. (c) and (d) show the distribution of afterslip and the shear stress recovery $\Delta\tau_c/\Delta\tau_p$ on the coseismic rupture. Arrows on each afterslip patch show the slip vector and are scaled by the afterslip amplitude.

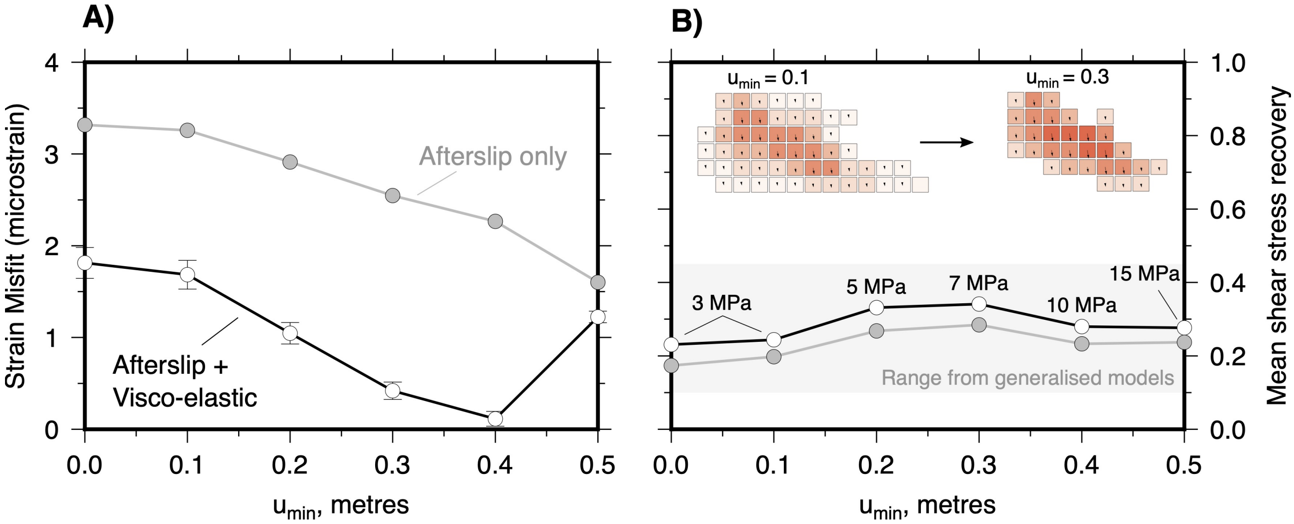

Figure 9: Calculations showing the effect of compacting the slip distribution on the observed surface strain and shear stress recovery. (a) Misfit between the observed and modelled across-fault extensional strain as a function of u_{min}. The misfit is calculated as: $1/n_j \sum_j \left[(\varepsilon^{mod}_{min} - \varepsilon^{obs}_{min})^2\right]^{1/2}$, where ε^{mod}_{min} is the modelled minimum principal strain amplitude and ε^{obs}_{min} is the observed minimum principal strain amplitude in the triangles $j = \{1, 2, ..., n_j\}$ that span the Mochiyama Fault. Error bars are ± 0.3 microstrain, but are not shown for the afterslip-only models. (b) Mean shear stress recovery over the whole rupture area. The grey background is the range of shear stress recovery inferred from the generalised models. Numbers above each point represent the fault-averaged stress drop for the slip model used to calculate the coseismic stress changes. Examples of the slip models are shown in the top half of the figure for $u_{min} = 0.1$ m and $u_{min} = 0.3$ m.

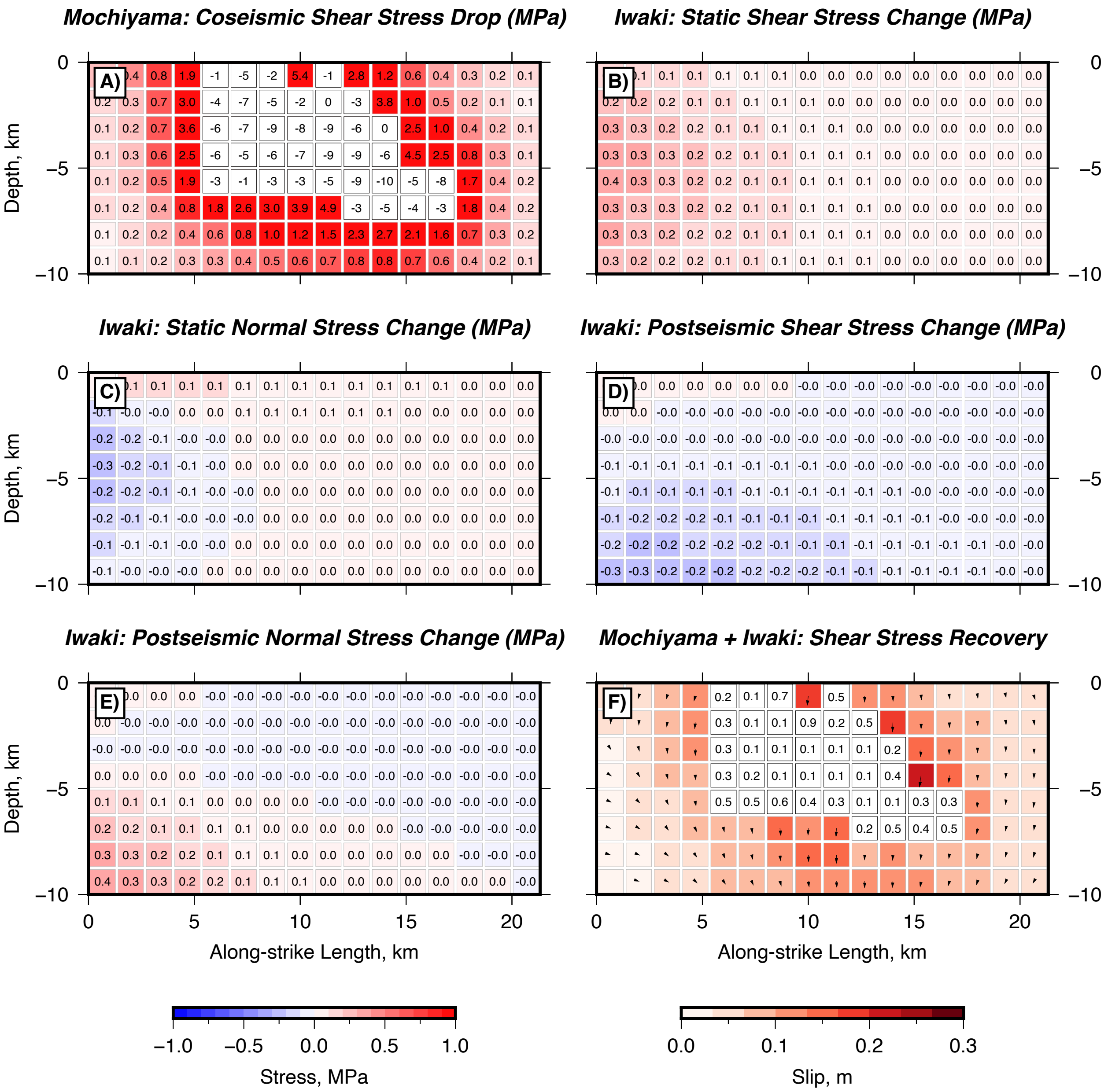

Figure 10: Contribution of the static deformation and postseismic relaxation associated with the Iwaki earthquakes to reloading of the Mochiyama Fault. By convention, shear stress changes are positive if the fault is loaded in the direction of slip and normal stress changes are positive for fault clamping. (a) Coseismic shear stress changes from slip on the Mochiyama Fault only. Shear stress (b) and normal stress (c) changes on the Mochiyama Fault due to coseismic slip in the Iwaki earthquakes. Shear stress (d) and normal stress (e) changes due to postseismic relaxation following the Iwaki earthquakes. (f) The pattern of afterslip and shear stress recovery on the Mochiyama Fault due to the relaxation of coseismic stress changes in models that include slip on both the Mochiyama and Iwaki faults. Colour scale for afterslip is the same as that in Figure 8.

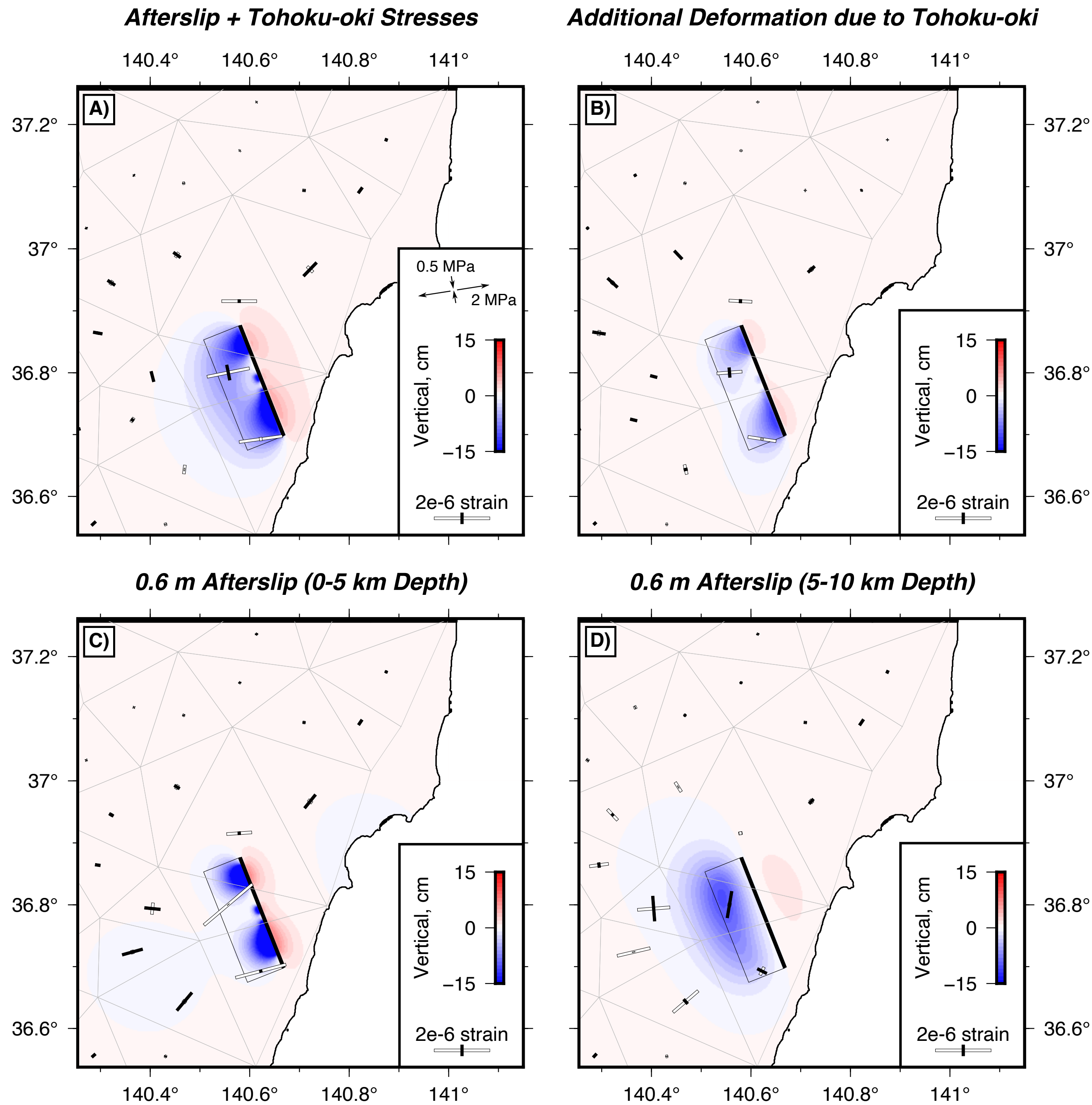

Figure 11: Effect of the Tohoku-oki earthquake on the postseismic deformation around the Mochiyama Fault. (a) Surface strain predicted by a model in which both the coseismic stress changes due to slip in the 2011 Mochiyama earthquake, and the stress changes due to co- and postseismic deformation from the Tohoku-oki earthquake, are relaxed by slip on the Mochiyama Fault. The principal stress changes caused by co- and post-seismic deformation in the Tohoku-oki earthquake from the model of Hu et al. [2016] are shown in the legend. (b) Difference between the model in (a) and the model in Figure 8b, showing the additional surface deformation caused by the Tohoku-oki earthquake. (c) Forward model of the strain predicted for 0.6 m of shallow afterslip on the top 5 km of the Mochiyama Fault around the edges of the coseismic rupture. The rake of the afterslip is in the same direction to coseismic slip. (d) Same as (c) but for 0.6 m of slip in the bottom 5 km of the Mochiyama Fault. (c) and (d) show that, to account for the observation of contractional strain within GPS triangles in the fault hangingwall over the inter-event period, the majority of the afterslip must have been relatively shallow.

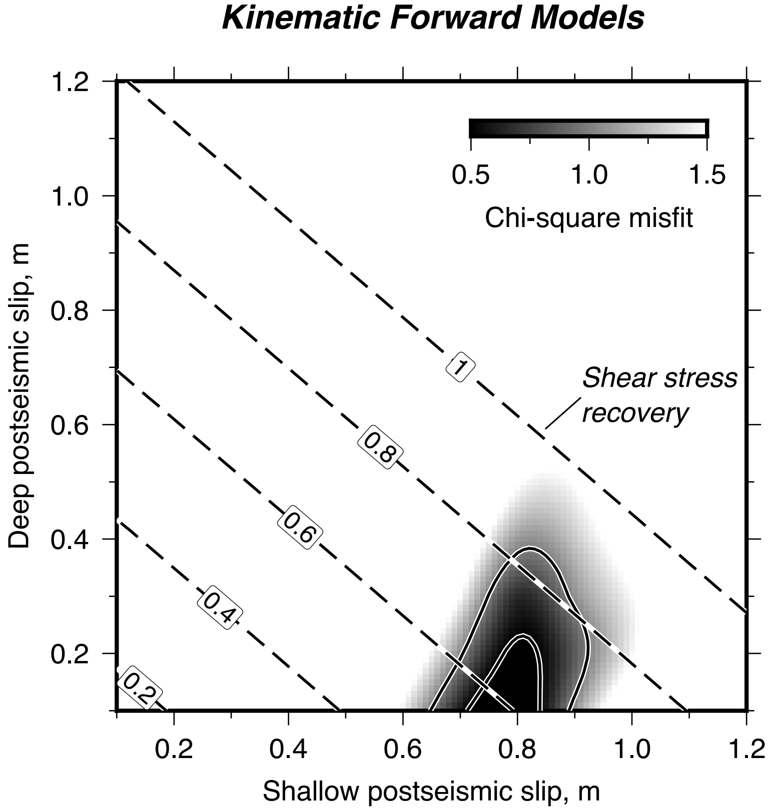

Figure 12: Kinematic forward models for the amount of shallow and deep triggered slip needed to account for the inter-event strain observations. The misfit between the models and the observations is expressed as the chi-squared misfit (χ^2), which is calculated as: $\chi^2 = 1/N \sum_{ij} \left[(\varepsilon_{ij}^{obs} - \varepsilon_{ij}^{mod})/\sigma \right]^2$, where $i = \{xx, xy, yy\}$ is the strain component, $j = \{1, 2, ..., n_j\}$ is the strain triangle, $N = 3n_j$ and σ is the uncertainty that we take to be 0.3 microstrain. We calculate the misfit for triangles that span the fault and that are within the fault hangingwall. The solid black lines represent the $\chi^2 = 0.5$ and $\chi^2 = 1.0$ contours. The dashed black lines show the mean shear stress recovery on the rupture area for the given amount of shallow and deep triggered slip. Models that match the observed strain have predominantly shallow slip, and an average shear stress recovery between 50% and 80% of the shear stress drop.

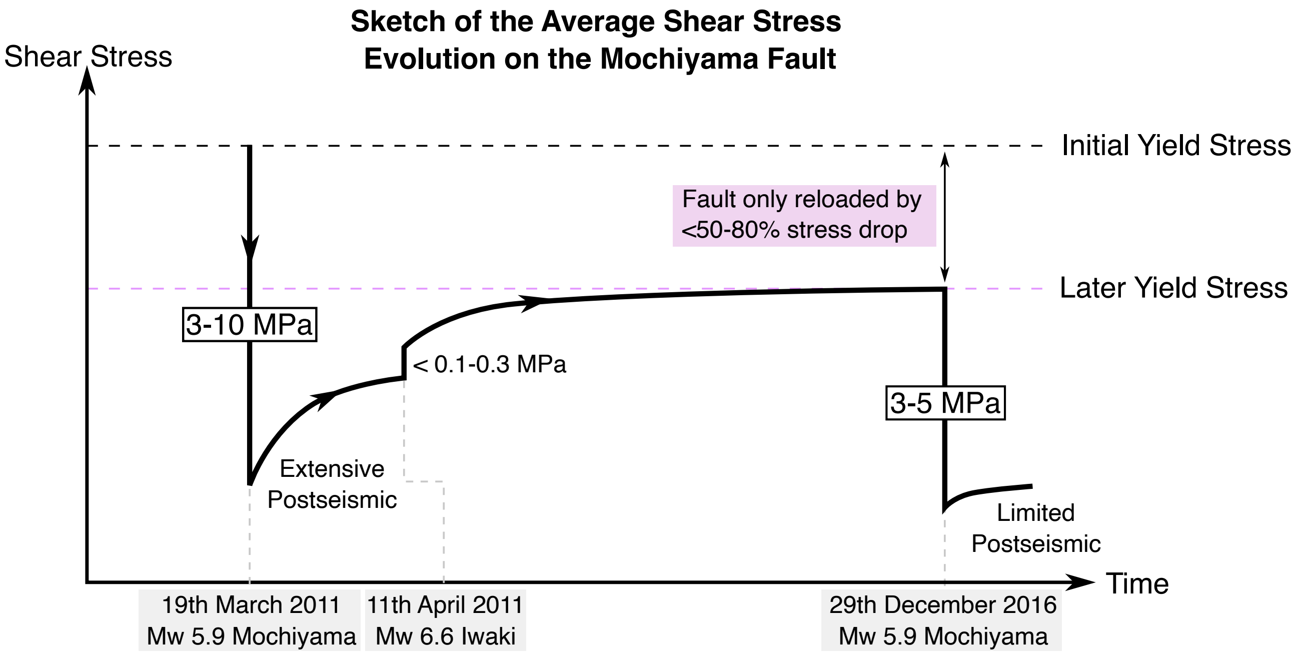

Figure 13: Sketch of the evolution of the fault-averaged shear stress on the Mochiyama Fault between the 2011 and 2016 earthquakes. The stress drop in the 2011 earthquake and 2016 earthquakes are shown in black boxes, and were calculated from the slip distributions of Fukushima et al. [2018].